

Article

Gold in Mineralized Volcanic Systems from the Lesser Khingan Range (Russian Far East): Textural Types, Composition and Possible Origins

Nikolai Berdnikov ^{1,*} , Victor Nevstruev ¹, Pavel Kepezhinskas ^{1,2} , Ivan Astapov ¹  and Natalia Konovalova ¹

¹ Kosygin Institute of Tectonics and Geophysics, Russian Academy of Sciences, 680000 Khabarovsk, Russia; nevstruevvg@mail.ru (V.N.); pavel_k7@yahoo.com (P.K.); astapov-itig@mail.ru (I.A.); turtle_83@mail.ru (N.K.)

² PNK Geoscience, Tampa, FL 33647, USA

* Correspondence: nick@itig.as.khb.ru; Tel.: +7-914-773-2625

Abstract: While gold partitioning into hydrothermal fluids responsible for the formation of porphyry and epithermal deposits is currently well understood, its behavior during the differentiation of metal-rich silicate melts is still subject of an intense scientific debate. Typically, gold is scavenged into sulfides during crustal fractionation of sulfur-rich mafic to intermediate magmas and development of native forms and alloys of this important precious metal in igneous rocks and associated ores are still poorly documented. We present new data on gold (Cu-Ag-Au, Ni-Cu-Zn-Ag-Au, Ti-Cu-Ag-Au, Ag-Au) alloys from iron oxide deposits in the Lesser Khingan Range (LKR) of the Russian Far East. Gold alloy particles are from 10 to 100 μm in size and irregular to spherical in shape. Gold spherules were formed through silicate-metal liquid immiscibility and then injected into fissures surrounding the ascending melt column, or emplaced through a volcanic eruption. Presence of globular (occasionally with meniscus-like textures) Cu-O micro-inclusions in Cu-Ag-Au spherules confirms their crystallization from a metal melt via extremely fast cooling. Irregularly shaped Cu-Ag-Au particles were formed through hydrothermal alteration of gold-bearing volcanic rocks and ores. Association of primarily liquid Cu-Ag-Au spherules with iron-oxide mineralization in the LKR indicates possible involvement of silicate-metallic immiscibility and explosive volcanism in the formation of the Andean-type iron oxide gold-copper (IOCG) and related copper-gold porphyry deposits in the deeper parts of sub-volcanic epithermal systems. Thus, formation of gold alloys in deep roots of arc volcanoes may serve as a precursor and an exploration guide for high-grade epithermal gold mineralization at shallow structural levels of hydrothermal-volcanic environments in subduction zones.

Keywords: Russian Far East; gold alloys; mineralized volcanic systems; spherules; explosive volcanism; liquid immiscibility; iron oxide copper-gold deposits; subduction zones



Citation: Berdnikov, N.; Nevstruev, V.; Kepezhinskas, P.; Astapov, I.; Konovalova, N. Gold in Mineralized Volcanic Systems from the Lesser Khingan Range (Russian Far East): Textural Types, Composition and Possible Origins. *Geosciences* **2021**, *11*, 103. <https://doi.org/10.3390/geosciences11020103>

Academic Editors:
Jesus Martinez-Frias and
Roberto Moretti

Received: 21 January 2021
Accepted: 15 February 2021
Published: 20 February 2021

Publisher's Note: MDPI stays neutral with regard to jurisdictional claims in published maps and institutional affiliations.



Copyright: © 2021 by the authors. Licensee MDPI, Basel, Switzerland. This article is an open access article distributed under the terms and conditions of the Creative Commons Attribution (CC BY) license (<https://creativecommons.org/licenses/by/4.0/>).

1. Introduction

Previous studies have established a firm link between gold mineralization and magmatic-hydrothermal processes and have shown close genetic and paragenetic relationship between gold and intrusive igneous activity [1–12]. Volcanic processes also appear to play significant role in gold transformations at the upper crustal levels, as native gold and gold-bearing alloys occur in lava flows of basaltic to dacitic composition [13–17], gas vents and fumaroles [18–23] as well as volcanic ash plumes [19,24–27]. The presence of native gold in ultramafic rocks [28–30] along with bulk-rock gold enrichments in some mantle peridotites [31–34] and crustal plutonic complexes [35–37], indicate that gold is transported from lithospheric mantle sources through magmatic plumbing conduits and finally concentrated at economic levels in epithermal environment [16,19,38–44]. Although gold appears to behave as an incompatible element during magmatic differentiation under

certain conditions [45–48], its geochemical behavior is strongly controlled by sulfur and oxygen fugacity in most magmatic-hydrothermal systems [49–53]. In general, gold is scavenged into sulfides in sulfur-rich, mafic to intermediate magmas [54–58] and is deposited as native metal or intermetallic compound in presence of reduced fluids [14,15,17,38,39,47]. The formation of native gold and gold-bearing alloys in magmas and volcanic systems is still a poorly documented and ambiguously understood phenomenon, which requires further constraints both from representative suites of natural samples as well as experimental studies. Specifically, the data concerning textures and compositions of gold and gold-bearing alloys in the early-stage magmatic plumbing systems are conspicuously lacking as most available information is related to the later-stage epithermal environments. This obvious gap in our knowledge of gold behavior in fluid-saturated igneous systems can be explained by high mobility of gold and, consequently, by almost complete replacement of magmatic gold with secondary textural and compositional forms during evolution of gold mineralization in hydrothermal settings. Therefore, the best conditions for the preservation of magmatic gold forms can be expected in igneous rocks that experienced fast cooling or quenching without substantial later-stage hydrothermal impact. These rocks include, first and foremost, various volcanic and sub-volcanic formations such as explosive breccias, ignimbrites and various tuffs.

We present in this paper results of study of gold micro-particles in iron oxide ores and associated volcanic rocks from Poperechnoye, Kostenga and Kaylan iron oxide (with manganese) deposits of the Lesser Khingan Range (LKR) ore province in the Russian Far East. Previous studies established significant role of mafic to felsic volcanism in the formation and evolution of these mineral deposits [59–61]. We also discuss possible models for origin and evolution of gold in deep-seated crustal magmatic systems with special emphasis on formation of gold deposits in volcanic environments.

2. Tectonic Background

The Poperechnoye, Kostenga and Kaylan deposits, together with more than 30 smaller deposits and showings, are part of an extensive cluster of iron oxide and iron-manganese mineralization within the LKR metallogenic province [62,63]. These deposits and mineral prospects are hosted in Vendian-Cambrian carbonate units of the Bureya-Jiamusi-Khanka composite terrane (Figure 1), which forms the easternmost segment of the Central Asian Orogenic Belt [61,64,65].

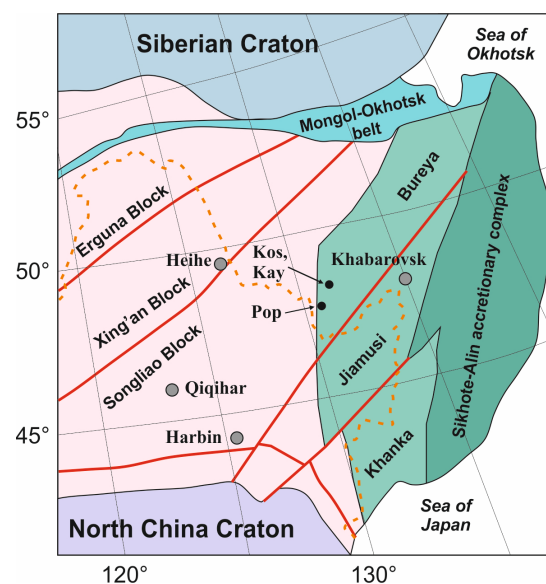


Figure 1. Tectonic setting of the Poperechnoye (Pop), Kostenga (Kos) and Kaylan (Kay) iron oxide deposits in the Russian Far East modified after [66]. Yellow dashed line depicts state border between China and Russian Federation.

One of the main geologic features of these iron-oxide deposits is the widespread occurrence of volcanic rocks such as explosive breccias, tuffs, lavas and sub-volcanic bodies.

3. Materials and Methods

Representative samples of iron-oxide mineralization and associated volcanic rocks from the LKR Fe-Mn deposits were collected by the authors during 2018–2019 field work. Substantial amount of the data presented in this study has been obtained on samples from earlier exploration workings and stored at the DV TFGU (Regional Fund of Geological Information, Khabarovsk, Russian Federation). All samples were collected inside freshly cut exploration trenches to avoid any possibility of anthropogenic contamination. Gold-bearing particles were liberated from the host iron-oxide ore and volcanic rocks through crushing to 0.25 mm followed by separation into various size fractions and washing with water. Heavy liquid separation and dissolution of excessive magnetite, hematite and carbonate in hydrochloric acid was applied to some samples in order to increase the amount of heavy mineral concentrate. Heavy concentrates were then hand picked under the Discovery V.12 stereomicroscope (Carl Zeiss, Oberkochen, Germany). Thin section studies were carried out using Imager A2m petrographic microscope (Carl Zeiss, Oberkochen, Germany).

A systematic study of gold-bearing grains was done using a VEGA 3 LMH TESCAN (Brno, Czech Republic) scanning electron microscope with the Oxford X-Max 80 (GB) EDS spectrometer (High Wycombe, UK, accelerating voltage—20 kV, beam current—530 pA, beam diameter—0.2 μm). A set of reference materials including 37 natural and synthetic oxides, minerals and metallic chemical elements (Oxford/108699 #6067) was used as reference standards; Co-standard Oxford Instruments/143100 #9864-15 was used for routine daily instrument calibration. The EDS compositions are considered to be precise within approximately ± 0.1 mas.%. X-ray diffraction (XRD) analysis of gold-bearing particles was conducted using the Miniflex II diffractometer (Rigaku, Tokyo, Japan) under the following set of conditions: $\text{Cu}_{K\alpha}$ -radiation, accelerating voltage of 30 kV and beam current of 15 mA.

Major element compositions of the bulk ore sample were determined on pressed pellets using a S4 Pioneer XRF spectrometer (Bruker, Billerica, MA, USA). International—LDI-3 (gabbro) and WMG-1a (mineralized gabbro)—as well as Russian—DVB (basaltic andesite), DVA (andesite) and DVD (dacite)—reference standards were used for calibration. Analytical uncertainty for major elements is $\pm 10\%$. Trace element abundances were measured using an ELAN 9000 ICP-MS (Perkin Elmer, Waltham, MA, USA), after an acid digestion of sample powder. The same set of rock reference standards (LDI-3, WMG-1a, DVB, DVA and DVD) along with Perkin Elmer standard solutions PE# N9300231–9300234 were used to monitor analytical accuracy and precision. The accuracy was $\pm 5\%$ for the trace elements with abundances of >20 ppm and $\pm 10\%$ for elements with abundances of <20 ppm. Additional details of analytical methods utilized in this study are reported in [61]. All analytical procedures were carried out at the Khabarovsk Innovative-Analytical Center (KhIAC) of the Kosygin Institute of Tectonics and Geophysics (Khabarovsk, Russian Federation).

4. Geology, Petrology and Geochemistry

Iron-oxide mineralization at the Poperechnoye deposit is represented by silicic hematite-magnetite ores and associated breccias containing up to 20–35 wt.% of total iron. Fe-oxide (with manganese) ore is concentrated within narrow (50–70 m) sub-longitudinal zone and can be subdivided into two sub-units: 1) Mn-rich (1 to 10 m thick) and 2) Fe-rich (up to 25 m thick) [61]. Ores are composed of dolomite, Mg-siderite, chlorite, quartz, magnetite, hematite with minor apatite, albite, orthoclase and rare grains of barite, monazite and xenotime. Manganese minerals include braunite and pyrolusite.

Breccias are essentially hybrid explosive rocks with andesitic to dacitic matrix with fragments of host dolomites, as well as earlier generation iron-oxide ores and breccias ranging in size from fractions of a millimeter to several tens of centimeters. These explosive breccias do not display any evidence for sorting or clastic sediment compaction (Figure 2).

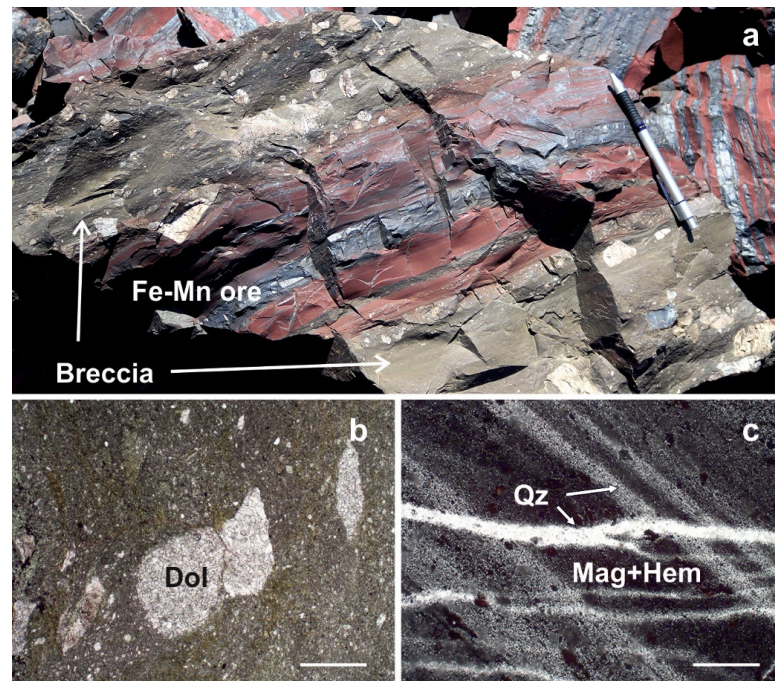


Figure 2. Iron-manganese ore at the Poperechnoye deposit associated with volcanic explosive breccia: (a) field photograph, thin section microphotographs of explosive breccia (b) and iron-oxide ore (c). Scale in photos b and c is 40 μm .

Explosive breccia and iron-oxide ore from the Poperechnoye deposit contain high concentrations of platinum-group metals (up to 11.3 ppm) and gold (up to 2.5 ppm) [59], which were interpreted as the result of contamination of fluid-saturated magma by PGE- and Au-rich material from the deeper levels of sub-continental lithosphere underlying Bureya-Jiamusi-Khanka terrane [61].

Fe-oxide mineralization along the eastern flank of the Poperechnoye deposit is associated with steeply dipping basaltic bodies (Figure 3a,b), which are replaced by mineralized breccias towards the southern terminus of the Poperechnoye deposit. Preliminary drilling completed within the deposit in 1955 by M.V. Chebotarev and his exploration team suggests that basaltic bodies converge at depth with primary ore bodies and associated (variably mineralized as well) explosive breccias. Basalts display typical porphyritic texture with phenocrysts composed of olivine, orthopyroxene, clinopyroxene, amphibole and plagioclase (almost completely replaced by secondary albite). Accessory minerals include ilmenite, magnetite, Fe-Cr spinel (occasionally with Ni), zircon, sulfides (pyrite, pyrrhotite, chalcopyrite) and apatite. Secondary alteration assemblages are dominated by albite replacing plagioclase and actinolite, tremolite, chlorite and sericite replacing iron-magnesian silicates, as well as hematite and various carbonates (calcite, dolomite, siderite) in the groundmass.

Several small peculiar carbonatite-like rocks are associated with iron-manganese mineralization and explosive breccias. They form sub-vertical, stock-like bodies up to 15 m in width, which elevate over 10 m above the surrounding erosional edifice, and are mostly composed of dolomite with minor olivine, orthopyroxene, fluor-apatite, corundum, vanadium-bearing and chrome-bearing magnetite and titanomagnetite, plagioclase, rutile, tremolitic-actinolitic amphibole, chlorite, pyrite, quartz and wollastonite (Figure 3c,d).

The iron-oxide ore at the Kostenga deposit is hosted in the Cambrian terrigenous-carbonaceous sediments and intruded by Ordovician granitoid and Middle to Late Carboniferous gabbroic complexes, as well as extensive felsic to intermediate dike swarms and Late Permian to Early Triassic granites. Along the northern edge of the Kostenga deposit, iron-oxide ore bodies are unconformably overlain by Cretaceous volcanic-sedimentary complexes including volumetrically important felsic tuffs and ignimbritic agglomerates and lava flows.

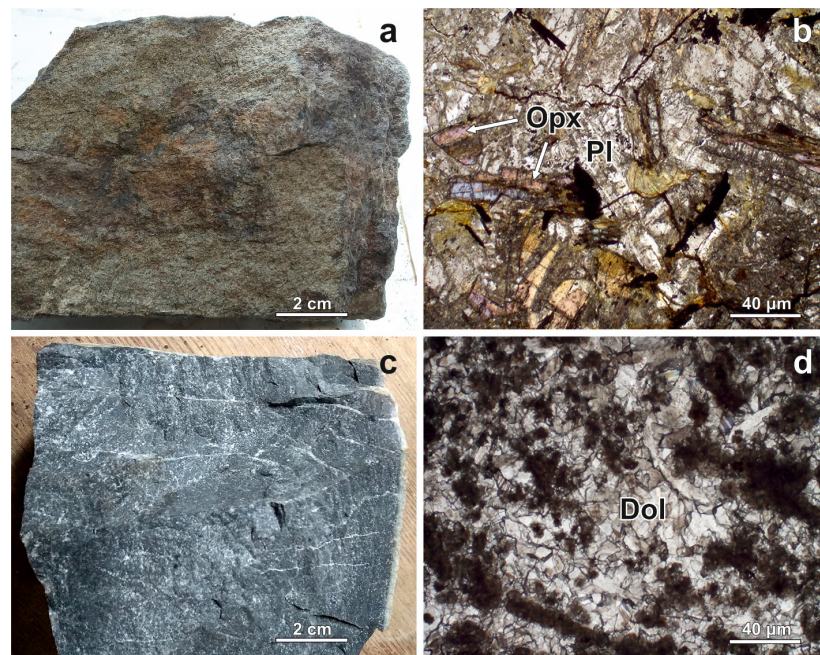


Figure 3. Basaltic (a,b) and carbonatite-like rocks (c,d) from the Poperechnoye deposit. (a,c)—hand specimens; (b,d)—thin section microphotographs.

Magnetite-hematite ores display laminated fluidal texture composed of lenticular quartz, magnetite, hematite, Fe-hydroxides and hydromica (Figure 4a,b). Minor constituents include chlorite, orthoclase, gedritic-gruneritic amphibole, stilpnomelane, apatite, monazite, Mn-minerals (pyrolusite and braunite). Textural features and mineralogical composition suggest primary magmatic origin for some samples of Kostenga iron-oxide ore (“magnetite lava”). Iron-oxide ore at the Kostenga deposit is closely associated with felsic explosive breccia containing fragments of host carbonates and iron-oxide ores (Figure 4c,d).

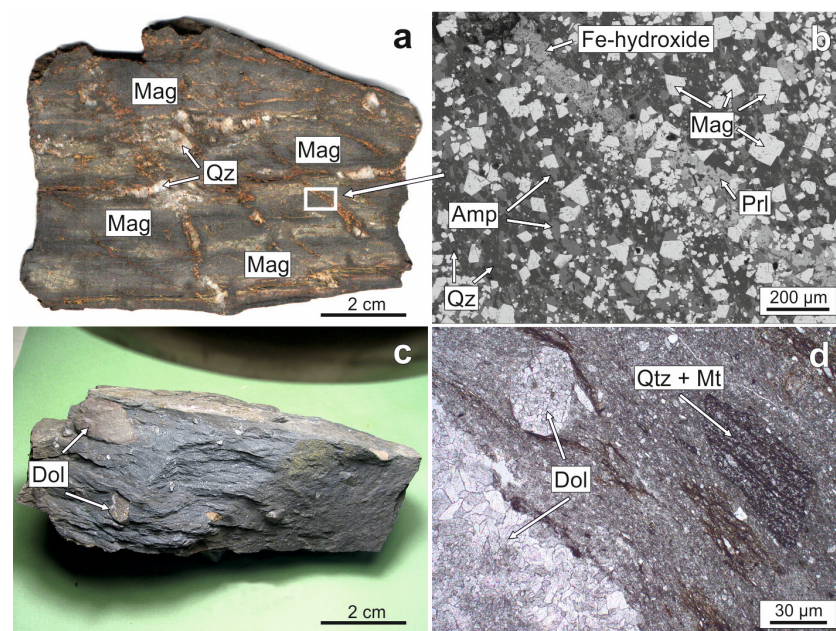


Figure 4. Iron-oxide ore (a,b) and explosive breccia (c,d) from the Kostenga deposit. (a,c)—hand specimens, (b)—SEM image, (d)—thin section microphotograph. SEM images here and throughout this manuscript were obtained in the backscatter electron (BSE) mode.

Kaylan Fe-oxide deposit is located approximately 10 km to the north-east from the Kostenga site (Figure 1). Mineralization straddles the contact between Upper Neoproterozoic (Vendian) dolomites and Lower Cambrian terrigenous-carbonaceous metasediments. Northern extension of the deposit is overlain by Cretaceous felsic to intermediate volcanics and tuffs, and the mineralization appears to be largely controlled by N-S-striking normal faults. Magnetite-hematite mineralization of the Kaylan deposit forms several isolated ore intervals with reduced thicknesses of 0.2 to 2.4 m. These ore bodies are composed of ferruginous tuffs (Figure 5a,b) and quartzites, as well as massive hematite ore. Fe-oxide mineralization at the Kaylan deposit are closely (both spatially and structurally) associated with explosive volcanic breccias and agglomerate tuffs (Figure 5c,d). Groundmass of these explosive volcanic rocks is composed of quartz, various carbonates, chlorite, tremolitic amphibole, mica and rare olivine. In some cases, altered matrix in volcanic breccia is composed of almost pure fine-grained hematite. Poorly sorted, unabraded and frequently deformed fragments of host carbonates along with minor quartz dominate clastic populations in both breccia and mineralized ore, suggesting genetic relationships between these two lithologies at the Kaylan deposit.

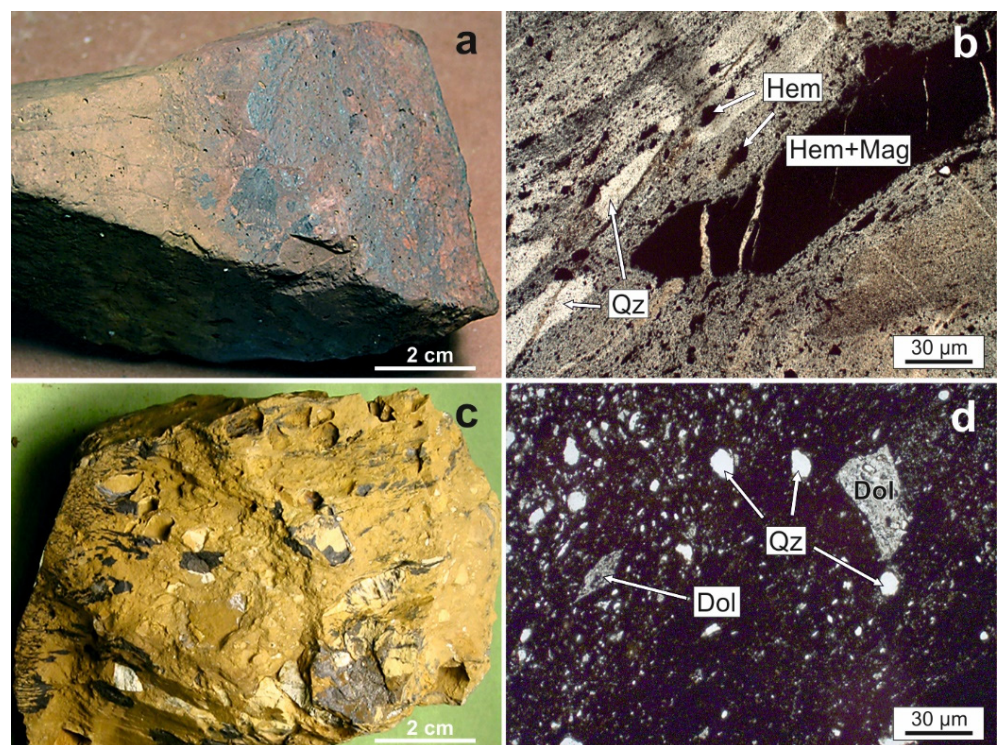


Figure 5. Hematite-rich (with magnetite) tuff (a,b) and breccia (c,d) from the Kaylan deposit. (a,c)—hand specimens; (b,d)—thin section microphotographs.

Chemical composition of igneous rocks and samples of mineralized ore from iron-oxide deposits in the Lesser Khingan Range are listed in Table 1.

Most ore samples as well as volcanic rocks have low-Ti chemical compositions with highly variable FeO, MgO and CaO contents (Table 1). Associated magmatic rocks display general sub-alkaline character, while explosive breccia samples from the Poperechnoye and Kostenga sites are characterized by elevated K₂O contents (2.34 and 1.81 wt.%, respectively; Table 1) approaching those typical of shoshonitic volcanic series [67,68]. Ores and volcanic rocks from the Lesser Khingan are enriched in large-ion lithophile (LIL) elements (although not without significant intra-element variations mostly attributable to secondary alteration and metasomatism) and display well-pronounced high-field strength (HFS) element depletions indicative of their subduction origins (Figure 6).

Table 1. Chemical composition of magnetite-hematite ores and magmatic rocks from the Poperechnoye, Kostenga, and Kaylan deposits.

Oxide/Element	Poperechnoye				Kostenga			Kaylan			
	Fe-Ore	Breccia	Carbonate.	Carb.- Like Rock	Basalt	Fe-Ore	Breccia	Tuff	Fe-Ore	Breccia	Tuff
SiO ₂ (wt.%)	48.32	50.68	7.77	9.39	52.08	65.85	41.39	49.98	39.06	54.79	57.75
TiO ₂	0.17	0.81	0.09	0.02	1.57	0.11	0.55	0.96	0.23	0.65	0.71
Al ₂ O ₃	2.24	11.37	0.87	0.22	10.46	1.88	8.60	11.43	2.47	9.27	9.81
Fe ₂ O ₃	38.32	9.02	1.68	1.88	10.72	26.67	6.86	8.38	48.29	16.31	11.15
MnO	0.50	0.18	0.15	0.87	0.13	0.99	1.27	0.13	0.22	2.19	3.92
CaO	2.79	6.88	29.35	29.68	4.72	0.69	11.43	6.26	0.67	3.08	3.24
MgO	3.47	7.02	18.11	16.49	10.93	1.52	9.65	7.75	2.46	1.80	1.33
Na ₂ O	0.58	1.08	0.25	0.00	5.54	0.10	0.11	0.37	0.14	0.21	0.21
K ₂ O	0.58	2.34	0.01	0.01	0.32	0.37	1.81	2.23	0.05	0.55	1.85
P ₂ O ₅	0.40	0.08	0.02	0.00	0.14	0.33	0.08	0.14	0.23	0.12	0.09
LOI	2.55	10.99	43.32 *	43.65 *	3.38	1.48	18.4	12.14	6.02	10.92	9.66
Total	99.93	100.45	101.61	102.21	99.98	99.99	100.16	100.49	99.85	99.91	100.00
Sc (ppm)	3.89	15.65	1.77	<0.001	17.96	3.48	10.00	22.31	6.75	11.51	14.47
V	40.65	62.58	15.31	0.38	134.24	47.78	96.09	167.88	59.33	132.59	149.56
Cr	21.45	34.57	16.77	5.03	356.63	22.84	75.78	135.74	17.95	83.27	78.57
Co	7.15	8.93	1.43	9.36	45.57	22.97	43.07	10.86	1.21	49.19	154.18
Ni	15.27	106.73	15.64	11.51	166.39	37.11	122.36	34.68	12.27	78.47	781.52
Cu	3.40	49.24	13.36	17.32	51.53	<0.001	23.89	25.00	12.67	31.28	146.84
Zn	27.96	73.3	18.24	24.77	127.97	32.89	65.06	78.53	27.61	57.15	81.38
Ga	2.52	15.24	1.65	0.30	19.92	2.07	11.66	13.64	4.55	15.08	16.38
Rb	28.22	89.67	8.93	0.31	8.10	31.42	60.70	92.67	2.20	24.05	76.19
Sr	61.63	56.54	99.30	67.96	208.9	41.88	85.74	94.04	11.31	36.96	48.88
Y	7.73	14.85	5.53	0.87	15.37	4.82	8.60	15.35	32.35	17.92	19.69
Zr	7.18	61.64	10.12	2.41	57.49	6.44	60.54	131.69	13.64	60.78	63.66
Nb	4.60	2.10	0.25	0.19	9.92	1.38	1.31	6.42	3.04	4.89	5.43
Ag	0.59	0.29	<0.001	0.07	0.16	2.44	0.62	0.81	0.33	0.50	0.26
Sn	0.23	1.99	0.11	<0.001	1.17	<0.001	1.38	2.74	0.05	1.84	2.44
Cs	6.73	4.17	0.40	0.09	2.54	18.91	2.20	3.84	0.57	4.00	6.13
Ba	107.22	557.71	69.81	47.79	308.44	822.80	824.37	498.14	82.09	151.73	220.81
La	3.87	21.43	3.62	0.49	6.11	2.31	21.56	30.84	11.91	23.86	28.03
Ce	9.11	48.44	7.94	1.00	13.81	4.83	42.25	63.81	20.77	47.08	56.70
Pr	1.19	5.46	0.95	0.11	1.84	0.68	5.21	7.85	3.63	5.92	6.77
Nd	5.53	23.56	3.89	0.44	8.73	2.96	19.67	30.65	16.40	21.71	23.51
Sm	1.26	5.02	0.86	0.09	2.67	0.71	3.76	5.75	3.82	4.06	4.58
Eu	0.26	0.91	0.20	0.03	1.02	0.19	0.73	1.04	0.97	0.69	0.88
Gd	1.56	4.93	1.05	0.12	3.57	0.87	3.62	5.27	5.04	4.21	4.93
Tb	0.22	0.63	0.15	0.02	0.56	0.13	0.41	0.61	0.77	0.57	0.73
Dy	1.53	3.63	0.85	0.10	3.19	0.78	2.00	3.06	4.83	3.11	3.92
Ho	0.31	0.64	0.17	0.02	0.60	0.16	0.38	0.58	1.07	0.64	0.80
Er	1.01	1.99	0.51	0.07	1.59	0.52	1.21	1.85	3.28	1.94	2.37
Tm	0.14	0.26	0.07	0.01	0.21	0.08	0.18	0.32	0.46	0.30	0.37
Yb	0.98	1.90	0.47	0.07	1.28	0.57	1.35	2.04	3.00	1.92	2.39
Lu	0.15	0.27	0.07	0.01	0.18	0.10	0.22	0.32	0.47	0.31	0.40
Hf	0.23	1.69	0.23	<0.001	1.80	<0.001	1.59	3.28	0.35	1.83	1.81
Ta	0.29	0.19	<0.001	<0.001	0.84	0.03	0.21	0.39	0.13	0.46	0.51
Pb	5.91	6.59	0.58	<0.001	2.33	0.79	15.03	2.34	4.35	9.24	18.00
Th	1.37	6.89	0.72	<0.001	0.68	0.77	6.24	9.48	1.47	6.94	7.31
U	0.36	0.52	0.16	0.00	0.21	0.27	1.08	3.94	1.65	1.85	2.60

Note: * High LOI in samples 3 and 4 is caused by carbonate decomposition.

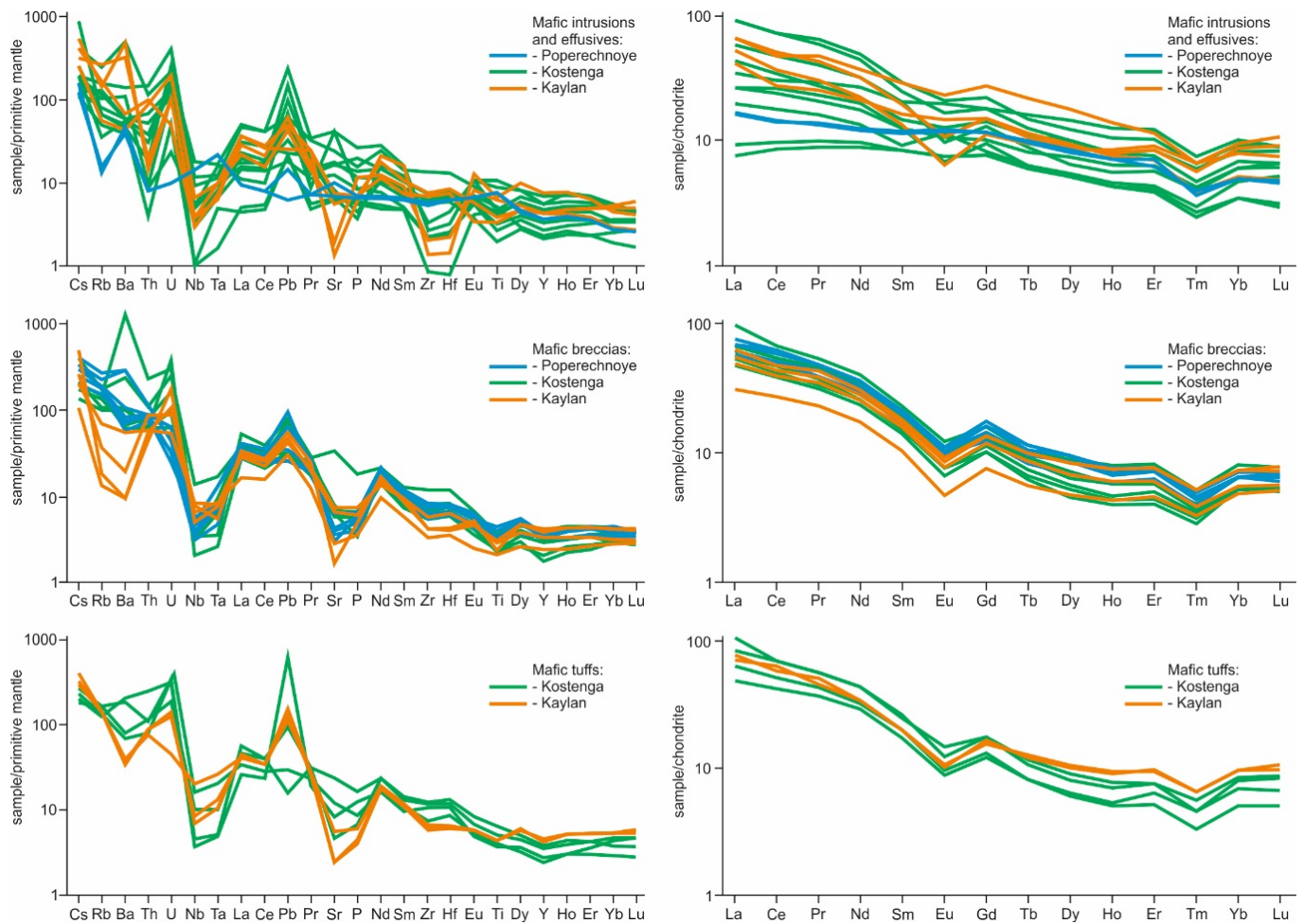


Figure 6. Primitive mantle-normalized [69] trace element (left column) and chondrite-normalized [69] rare earth element (right column) patterns for the volcanic rocks associated with the LKR iron-oxide deposits.

Most compositions are also characterized by distinctive negative Sr anomaly reflective of plagioclase fractionation during the course of magmatic differentiation of primary basaltic magma (Figure 6). All ores and volcanic rocks are enriched in light rare earth elements, with basaltic small intrusions displaying highest variability in La/Sm and La/Yb ratios (Figure 6). Most REE patterns are also characterized by prominent negative Eu and Tm anomaly. Some subtle variations in LILE and REE may be attributed to variable alteration and metasomatic processes that affected both ores and associated volcanic rocks from the LKR deposits. Trace element systematics suggests general affinity of the LKR igneous rocks with the volcanic arc, island arc and calc-alkaline basalts in Cr-Y (Figure 7a), Ti-Zr (Figure 7c), Nb/U-Nb (Figure 7d), Th-Zr-Nb (Figure 7e) and Th-Zr-Ta (Figure 7f) tectonomagmatic discrimination diagrams. The LKR rocks plot in or near the active continental margins field in the Th/Yb-Ta/Yb discrimination plot exhibiting rather significant Th/Yb variations (1 to 10; Figure 7b), which, again, may be a reflection of secondary chemical changes rather differences in mantle sources or differentiation processes. In addition, both ores and volcanic rocks from the LKR are characterized by uniformly low Nb/U ratios typical of modern arc basalts (Figure 7d). On the contrary, basalts from the Poperechnoye deposit display elevated HFSE concentrations (Nb = 9.92 ppm; analysis 5 in Table 1) and plot into the ocean island basalt (OIB) fields in some geochemical discrimination diagrams (Figure 7e,f).

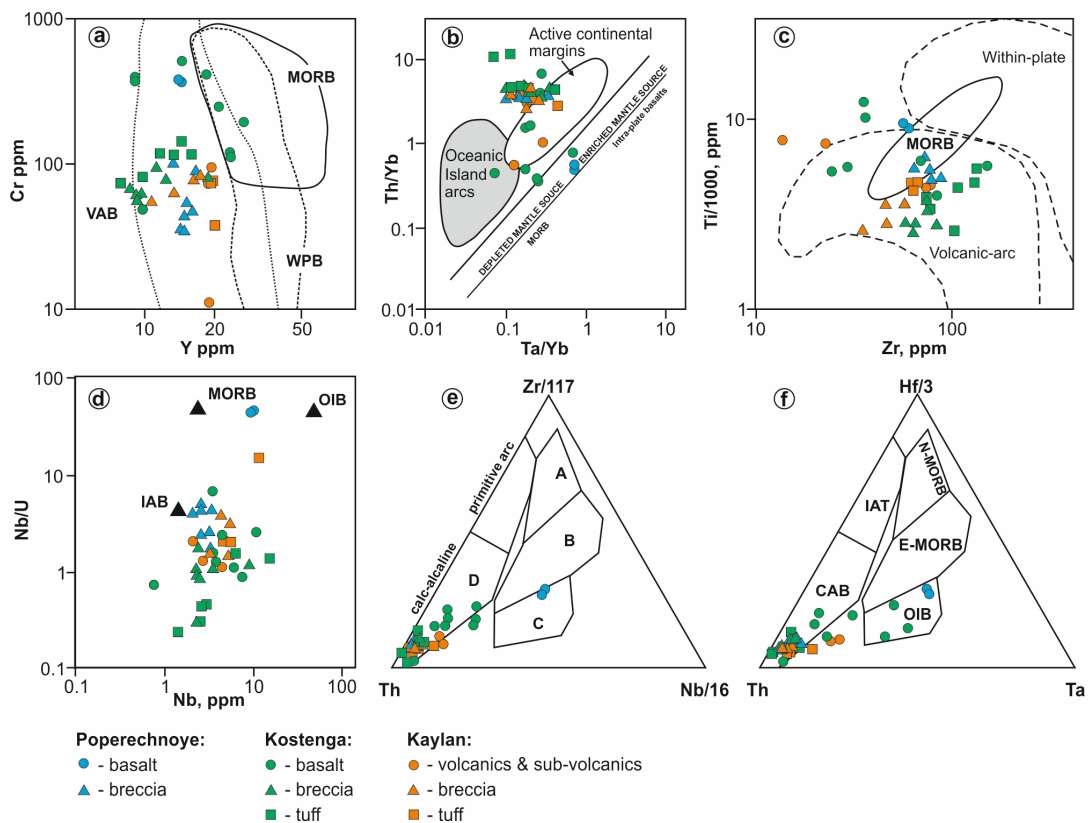


Figure 7. Tectonomagmatic discrimination diagrams for volcanic rocks associated with iron-oxide mineralization in the Lesser Khingan Range: (a) Cr–Y [70]; (b) Th/Yb–Ta/Yb [71]; (c) Ti–Zr [70]; (d) Nb/U–Nb [72]; (e) Th–Zr–Nb [73] (A—N-MORB, B—E-MORB, C—OIB, D—VAB); (f) Th–Hf–Ta [73]. VAB—Volcanic Arc Basalt, MORB—Mid-Ocean Ridge Basalt, WPB—Within-Plate Basalt, IAB—Island-Arc Basalt, OIB—Ocean Island Basalt, CAB—Calc-Alkaline Basalt, IAT—Island Arc Tholeiite, N-MORB—Normal (depleted) MORB, E-MORB—Enriched MORB.

5. Gold and Gold-Bearing Alloys in Ores and Igneous Rocks

Gold in studied samples from the three LKR deposits ranges in size from 10 to 100 μm, rarely over 200 μm and forms two distinct compositional and textural groups. The most numerous group (more than 200 studied grains) is represented by gold-silver alloys with gold contents ranging between 65 and 100 wt.% (Figure 8). These are mostly shapeless, lumpy, frequently elongated and flattened grains with homogeneous internal structure. They exhibit uneven surfaces, occasionally with some elements of surficial sculpture. The second group includes spherical grains with the following compositional ranges: Au = 55–70 wt.%, Ag = 0–13 wt.%, Cu = 30–45 wt.% (Figure 8). Most spherules from this group display “shagreen”-type sculptured surfaces with characteristic indentations formed during solidification and compaction of noble metal particles.

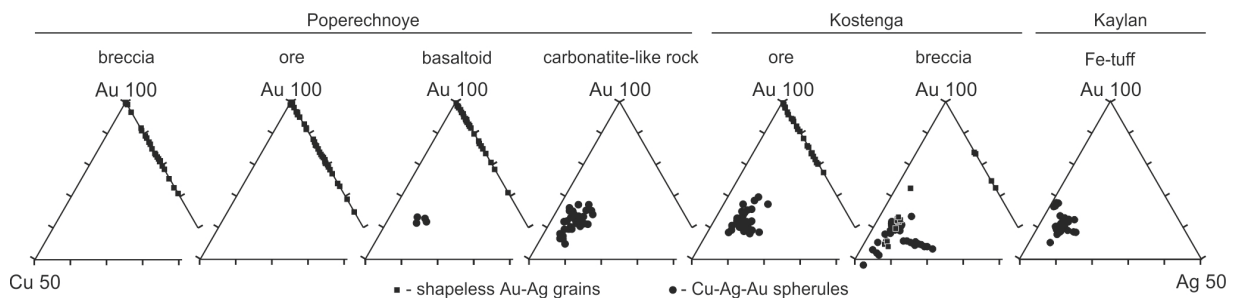


Figure 8. Composition of gold alloys from the three Lesser Khingan Range LKR Fe-oxide deposits and associated volcanic rocks.

5.1. Gold in Explosive Breccia and Fe-Oxide Ore of the Poperechnoye Deposit

A single sample of explosive breccia from the Poperechnoye iron-oxide deposit yielded 40 shapeless (with rare elements of surficial sculpture) and subordinate rounded and nodular grains of gold-silver alloys ranging in size from 70 to 150 μm (Figure 9). Gold content in these grains ranges from 70 to 100 wt.% (Figure 8). They typically have homogeneous internal structure and chemical composition. Several rounded grains exhibit overgrowth of native bismuth (with minor lead and tin) on pure gold particle (Figure 9f).

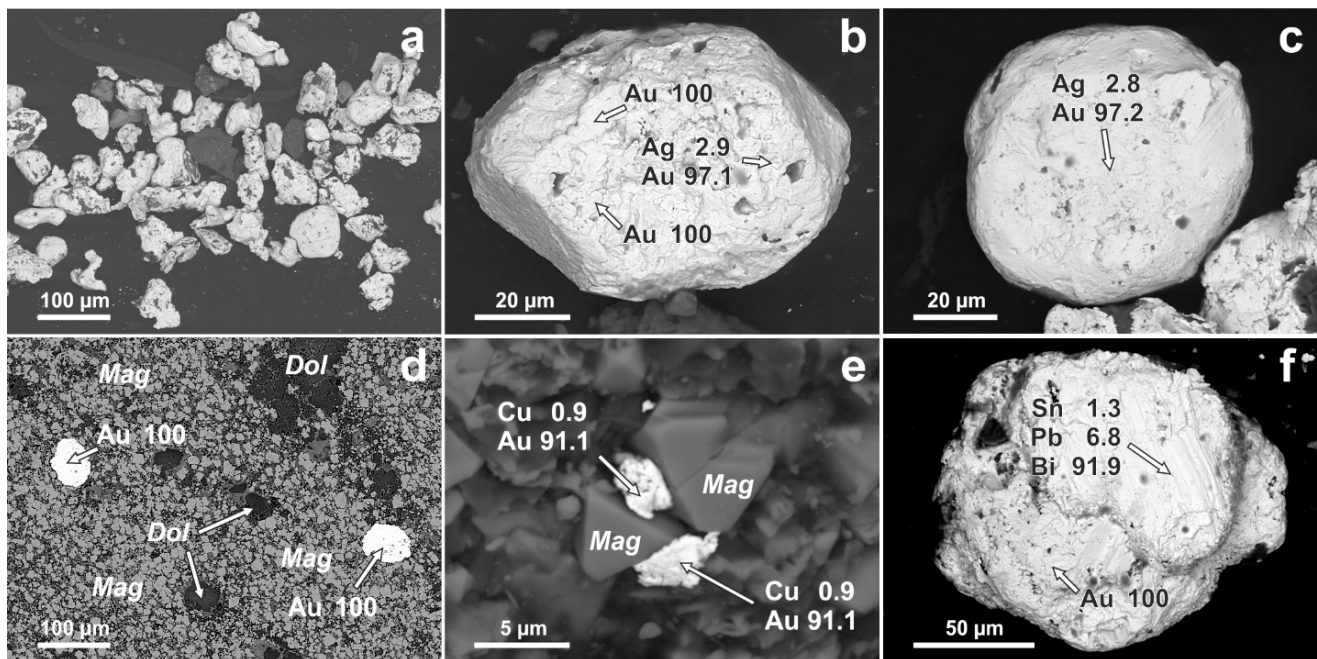


Figure 9. Gold-silver alloys and associated minerals in ores and explosive breccia from the Poperechnoye deposit: (a–c)—high purity gold of variable shape (a), subhedral (with retained crystal faces) (b) and rounded (c); (d,e)—gold grains in magnetite ore; (f)—native bismuth overgrowth on gold grain. Chemical analyses of alloys and minerals in all figures are in wt.%. Arrows indicate precise location of SEM-EDS data points.

More than 100 grains of gold-silver alloys were extracted from hematite-magnetite (with Mn) ore samples. These particles also range in size from 70 to 150 μm (Figure 9) and display homogeneous internal structure and bulk chemical composition. Their gold content ranges between 65 and 100 wt.% (Figure 8), with seven grains showing copper content of 0.6 to 3.9 wt.%. Minor palladium (5.9 wt.%) was detected in single gold-silver particle. Figure 9d,e demonstrates grains of pure (100%) or nearly pure (91%) gold particles included in magnetite ore in situ. Relatively large (>50 μm) rounded grains are imbedded in magnetite-quartz-dolomite matrix (Figure 9d), while smaller (3–5 μm) angular grains are clearly texturally associated with euhedral magnetite crystals (Figure 9e).

5.2. Gold in Basaltic Intrusion from the Poperechnoye Deposit

Two types of gold-bearing alloys were identified in steeply dipping basaltic body, which is associated with iron-oxide mineralization along the eastern flank of the Poperechnoye deposit. The most common (48 individual grains identified) are shapeless particles with overall subhedral to anhedral appearance (Figure 10a). Their composition varies from 71 to 100 wt.% Au (Figure 8).

Most gold particles of this type are internally homogeneous. Twelve gold grains out of 48 analyzed particles (25%) include minor iron (0.3–2.6 wt.%), five grains (10%) contain copper (0.5–0.6 wt.%) and one grains contains 1 wt.% of titanium. One rounded grain is enclosed in the pure (100 wt.% Au) gold rim, which contains micro-inclusions of euhedral monazite (Figure 10c). The core of the same spherule also includes euhedral

magnetite crystal (Figure 10b). Four grains display almost spherical shapes with sculptured surfaces (various indentations) consistent with compaction and solidification of previously molten material during cooling (Figure 10d). These grains are composed of copper (27–31 wt.%), silver (8–10 wt.%) and gold (61–64 wt.%) and are frequently covered with rims of predominantly copper-oxide and magnesium-silicate composition (Figure 10d). These spherules commonly display heterogeneous internal structures. The main volume of an individual spherule is composed of homogeneous (at the detection levels of our SEM-EDS instrumentation) alloy, which contains a) spherical inclusions (first microns in diameter) of mostly copper-oxide composition with minor iron admixture and b) larger (around 5 μm) spherical cavities. The latter are either partially empty, or contain dendritic formations, compositionally similar to the bulk spherule matrix (lower left part of the BSE image in Figure 10e). Some spherules display sharp and clear meniscus-like boundaries between Cu-Ag-Au core and copper-oxide rim (Figure 10e), as well as Cu-Ag-Au alloy and Cu-oxide partially encrusting some cavities in copper-silver-gold spherules (Figure 10f). Both textures are indicative of liquid immiscibility processes accompanying formation of these spherules.

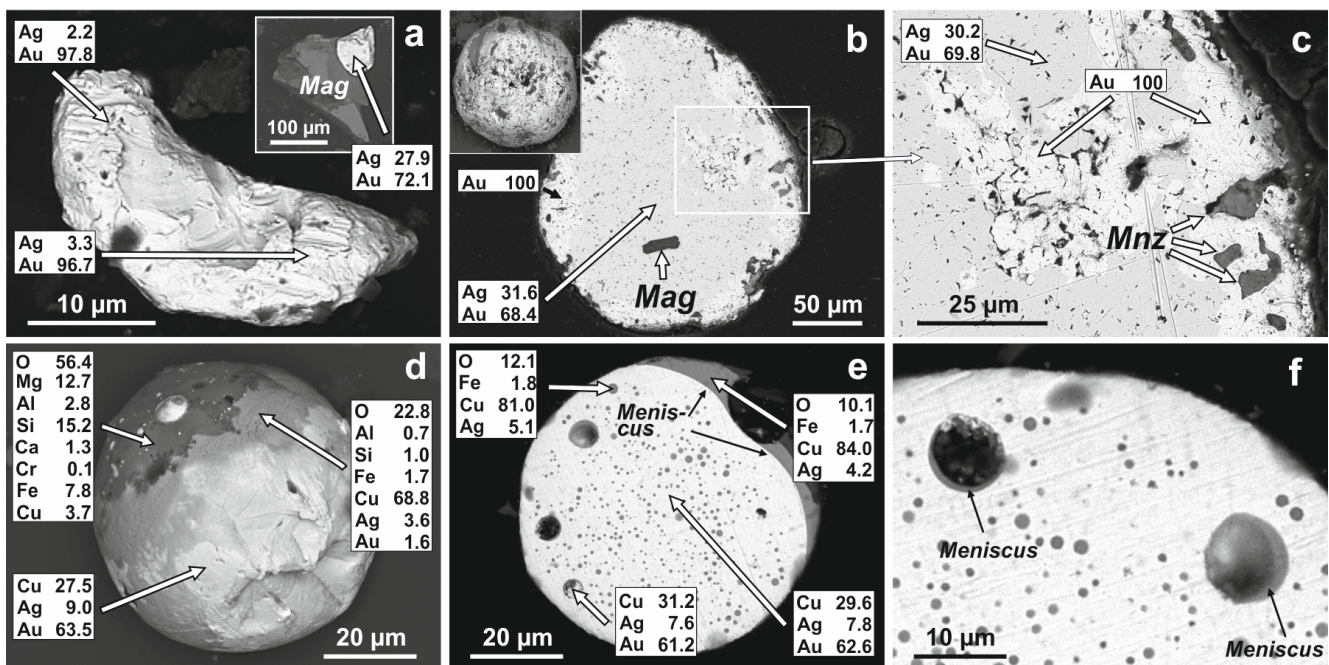


Figure 10. Gold-bearing grains in basaltic intrusion from the Poperechnoye deposit: (a)—shapeless particle with partially preserved original magmatic crystal faces and gold-silver alloy in association with magnetite (Mag) (inset); (b,c)—rounded particles (micro-spherules) with pure gold rims and inclusions of euhedral magnetite (Mag) (b) and monazite (Mnz) (c); (d)—Cu-Ag-Au micro-spherule with compaction-related deformations and copper oxide and magnesium-silicate outer shell (rim); (e,f)—internal structure of the spherule in (d) with abundant spherical cavities and copper-oxide micro-inclusions. Surface of the spherule (e) and some larger internal cavities (f) exhibit clear and sharp meniscus-like boundaries indicative of liquid immiscibility.

5.3. Gold in Carbonatite-Like Rocks of the Poperechnoye Deposit

Carbonatite-like rocks from the Poperechnoye deposit contain exclusively spherical gold-bearing alloys and no shapeless gold particles have been encountered so far. A total of 32 Cu-Ag-Au spherules ranging in size from 15 to 35 μm were extracted from these exotic formations at Poperechnoye (Figure 11). Gold spherules commonly feature abundant indentations indicative of compaction process that typically accompany solidification of previously molten material (Figure 11a).

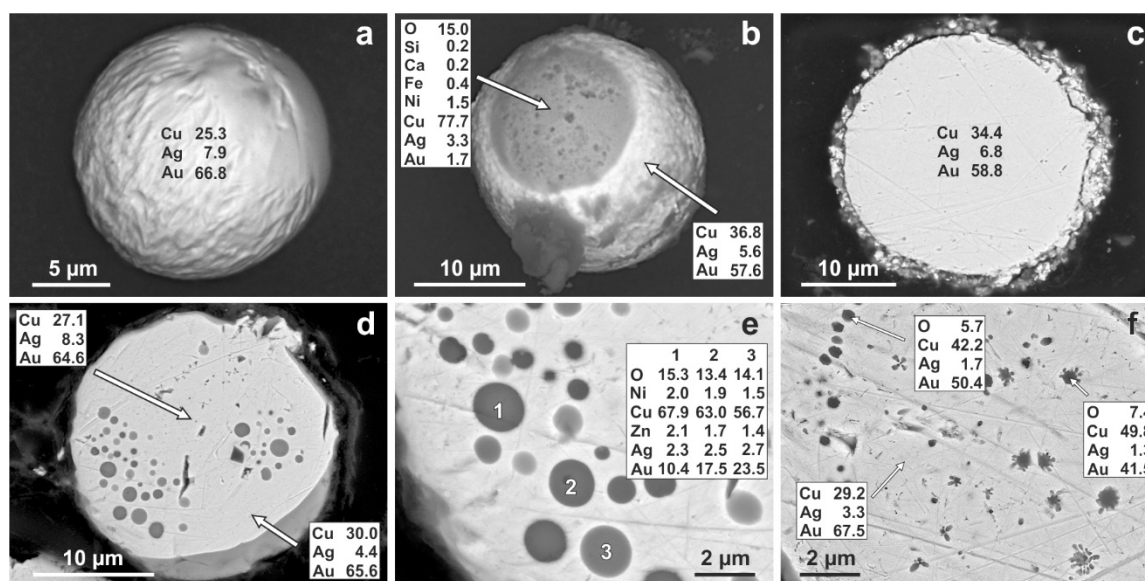


Figure 11. Gold-bearing spherules in carbonatite-like rocks from the Poperechnoye deposit: (a)—sculptured spherule exterior with multiple compaction-related deformations; (b)—internal structure of a homogeneous spherule; (c–f)—internal structures of gold-bearing spherules with copper oxide rim (c), and spherical (d,e) or dendritic (f) copper oxide inclusions.

Thirteen spherules carry rims, partially enclosing Cu-Ag-Au cores, composed of copper oxides (Figure 11b). Visually, precious metal cores and copper oxide rims form a single sphere with a clear convex meniscus-like boundary between the two phases (Figure 11d). Rims are composed of copper (35.6 to 86.5 wt.%; average of 65.8 wt.%) and oxygen (8.5 to 47.7 wt.%; average of 20.8 wt.%) along with iron (0.2 to 20.2 wt.%; average of 3.7 wt.%). In addition, our SEM-EDS study detected nickel (up to 8.2 wt.%; average of 1.6 wt.%) and silicon (up to 5.1 wt.%; average of 0.8 wt.%) in 10 out of 13 analyzed rims, zinc (up to 11.4 wt.%; average of 2.7 wt.%) in 8 rims, calcium (up to 1.5 wt.%; average of 0.3 wt.%) in 7 rims, sulfur (up to 0.7 wt.%; average of 0.7 wt.%) in 6 rims, chlorine (up to 3.6 wt.%; average of 0.6 wt.%) in 4 rims, aluminum along with potassium and titanium (up to 0.8, 0.6 and 4.2 wt.% respectively) in 3 rims and sodium together with chromium and indium (up to 7.5, 10.2 and 0.6 wt.%, respectively) in 2 rims. One copper oxide rim contains 1.0 wt.% of magnesium.

Precious metal spherules in carbonatite-like rocks either display homogeneous internal structure (Figure 11c) or contain abundant spherical copper oxide inclusions (Figure 11d,e). Homogenous Cu-Ag-Au spherules and matrices of spherules with spherical copper oxide inclusions appear to be compositionally similar with copper ranging from 26.4 to 37.5 wt.% (average of 31.9 wt.%), silver—from 2.2 to 13.6 wt.% (average of 5.4 wt.%) and gold—from 57.2 to 68.6 wt.% (62.7 wt.%) (89 total analyses; Figure 8).

Copper-oxide inclusions (Figure 11d–f) are also compositionally similar to the copper-oxide rims in composite (zoned) spherules (e.g., mostly copper and oxygen, with minor nickel and zinc). However, it is difficult to obtain representative compositions of copper-oxide micro-inclusions due to their extremely small dimensions. EDS analyses of micro-inclusions commonly include components from the precious metal matrix due to the commonly wider (in comparison with the micro-inclusion size) area excited by the analytical X-ray radiation (Figure 12). This results in various additions of Cu, Ag and Au to the individual inclusion compositions. This can be demonstrated, at least to a certain extent, by Figures 11e and 12, which show inclusions 1, 2 and 3 with progressively increasing cross-section (emphasized by increasing lighting of their BSE images) well correlated with changes in Au, Ag and Cu contents (specifically increase in Ag and Cu contents). Thus, analyses with lowest gold contents (gold is the most abundant metal

component of the spherule matrix) are considered as the best approximation for the bulk inclusion composition.

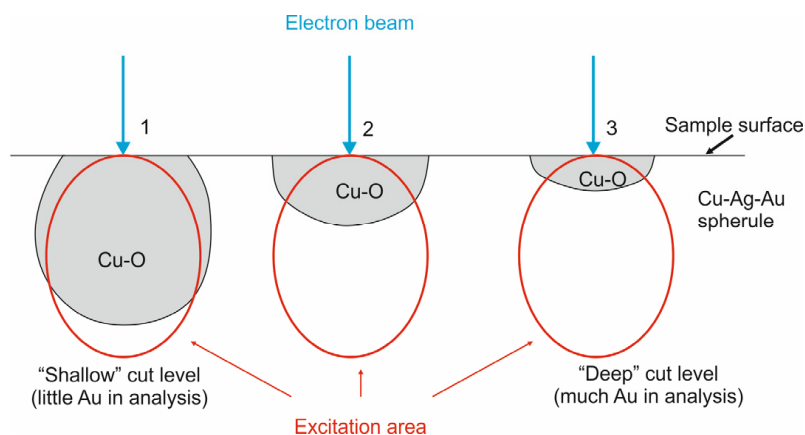


Figure 12. Dependence of gold concentrations in the EDS analyses of Cu-O micro-inclusions from the degree of exposure (cut level) of the individual Cu-Ag-Au spherule (a schematic illustration).

Along with spherical copper-oxide inclusions, Cu-Ag-Au spherules contain dendritic and irregular Cu-O segregations (Figure 11f). These segregations display higher copper and lower silver and gold contents coupled with ubiquitous presence of oxygen in their compositions. If, like in the case of spherical micro-inclusions, most of gold and silver in the relevant SEM-EDS analyses is due to the influence of the precious metals-rich matrix, predominantly copper-oxide composition of the dendritic segregations appears to be reasonably well-established by this study.

5.4. Gold in Ores and Pyroclastic Rocks from the Kostenga Deposit

Iron-oxide ores and associated pyroclastic rocks from the Kostenga deposit contain abundant gold-bearing alloys (a total of 90 grains were recovered in the course of this study; Figure 13). They commonly have lumpy or flattened appearance, occasionally with partially sculptured surfaces (Figure 13a,c), but some (total of 28 particles) have well-established spherical shape (Figure 13e–i). Shapeless (lumpy or flattened) grains are mostly composed of silver-gold alloy (51 grains) with gold content ranging from 72 to 100 wt.% (Figure 8). These Ag-Au alloys commonly have homogeneous internal structure. Some irregular grains (11 in total) are associated with yttrium-bearing baddeleyite (Figure 13c) and contain exsolution phases composed of Ti-Cu-Ag-Au intermetallic compounds (Figure 13c,d; Table 2).

Table 2. EDS compositions (wt.%) of gold-bearing alloys and related mineral phases in iron-oxide ore and pyroclastic rocks from the Kostenga deposit.

Element	1	2	3	4	5	6	7	8	9	10	11	12	13
O	3.6	5.0	4.7	6.5	9.1			25.5		9.7	11.1	6.9	17.1
Ti	0.7	13.1	11.9	1.9	39.3								
Cr										0.3		0.4	1.6
Fe		0.3						0.6					0.4
Ni								3.1		0.6	2.0		6.1
Cu	61.8	17.8	13.9	6.1	8.6	29.0	33.8	58.8	31.8	51.8	43.5	78.1	42.6
Zn	2.5							7.6			2.0		13.9
Ag	8.0	1.5	1.0	68.2	2.2	8.4	6.3	3.2	6.2	4.9	3.7	2.3	2.4
Au	23.5	62.2	68.5	17.3	40.8	62.7	59.9	1.2	61.9	32.7	37.8	12.3	15.8

Numbers of individual EDS analyses correspond to encircled data points in Figure 12. 1–5—Ti-bearing exsolution phases from irregular particles; 6, 9—matrix compositions from Cu-Ag-Au spherules; 7—composition of dendritic phase encrusting cavities in some spherules; 8—composition of partial rim on Cu-Ag-Au spherule; 10, 11—compositions of faceted (10) and dendrite-like (11) copper-oxide inclusions; 12, 13—analyses of the composite spherical copper-oxide inclusion with the meniscus-like texture in Figure 13h.

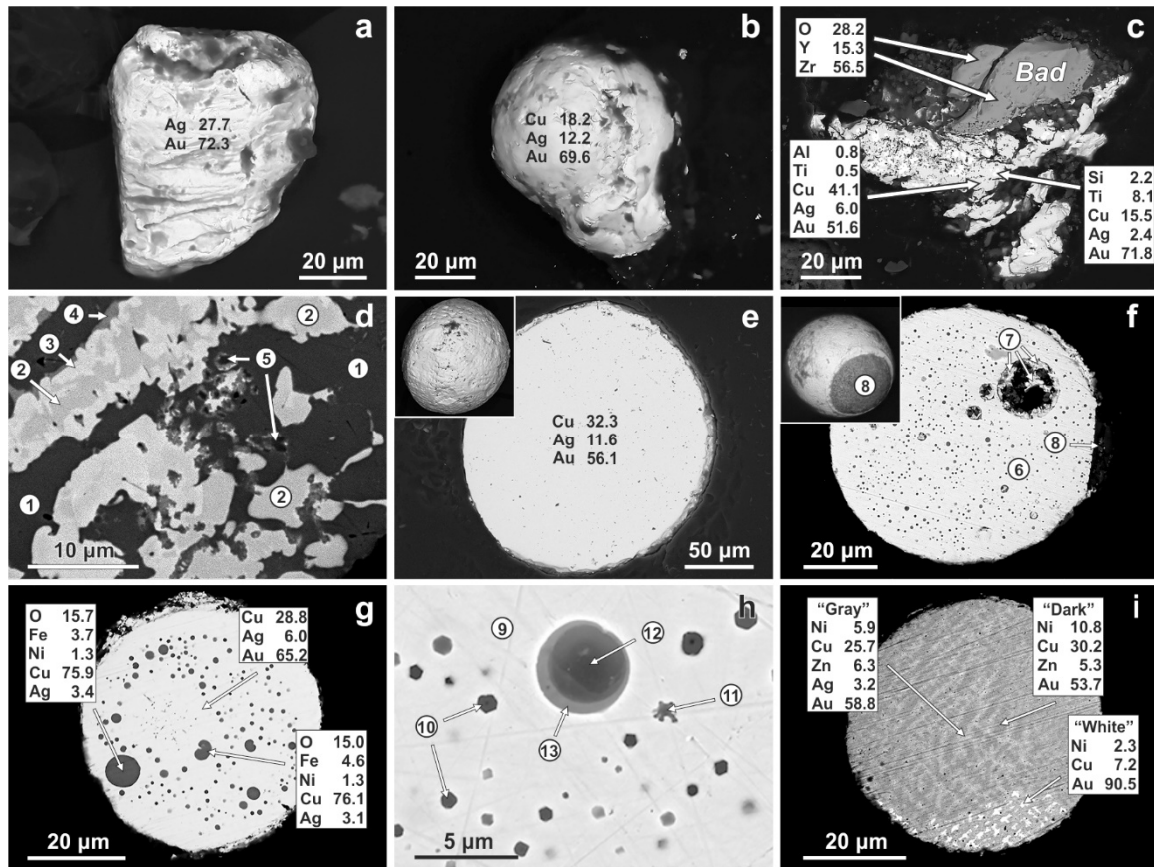


Figure 13. Gold-bearing alloys in explosive breccias (a,c–e) and iron-oxide ores (b,f–i) from the Kostenga deposit: (a)—irregular Ag-Au grain with elements of the surface sculpture; (b)—Cu-Ag-Au alloy with distorted spherical shape; (c)—highly irregular grain associated with baddeleyite; (d)—enlarged fragment of the internal structure of the grain shown in (c) with exsolved Ti-Cu-Ag-Au phases (points 1–5 correspond to EDS analyses in Table 2); (e)—internal structure of a homogeneous Cu-Ag-Au spherule; (f)—exterior view (inset) and internal structure of Cu-Ag-Au spherule with partial rim and spherical inclusions of Cu-rich composition, as well as spherical cavities encrusted with Cu-Ag-Au dendrites; (g)—cross-section of Cu-Ag-Au spherule with large spherical Cu-rich inclusions; (h)—cross-section of Cu-Ag-Au spherule with faceted and dendrite-like Cu-rich inclusions and a single, relatively large composite Cu-rich phase with meniscus-like texture; (i)—internal structure of Ni-Cu-Zn-Ag-Au spherule with exsolution textures. Numbers (data points) in figures a–i correspond to EDS analyses in Table 2.

Copper-silver-gold spherules (total of 28 recovered) range in size from 30 to 82 μm and commonly display solidification and compaction textures (Figure 13e–g). Some Cu-Ag-Au spherules exhibit surficial dendritic encrustations (Figure 13f,g) as well as fragments of partial rims with complex Cu-rich chemical compositions (Figure 13f; Table 2). Some of these spherules are internally homogeneous (Figure 13e) and display virtually no compositional differences between individual Cu-Ag-Au spherules (Figure 8). Analogously to the spherules from basaltic and carbonatite-like rocks from Poperechnoye deposit, Kostenga spherules contain rounded micro-inclusions ranging in size from fractions of a micrometer to 7.3 μm (Figure 13f–h). These spherical micro-inclusions are evenly distributed throughout the volume of individual Cu-Ag-Au spherules (Figure 13f), or concentrated along the spherule margins, still leaving very thin (~ 3 μm) outermost rims inclusion-free and chemically homogeneous (Figure 13g). The micro-inclusions and chemically similar partial rims on Cu-Ag-Au spherules are composed of copper oxide with minor iron, nickel and silver (Table 2).

Occasionally, some larger copper-oxide inclusions are characterized by meniscus-like texture, typically indicative [74–76] of solidified co-existing immiscible liquids (Figure 10h).

The two phases separated by the meniscus-like border display clear compositional differences: volumetrically predominant, darker (BSE colors) phase in the center of this inclusion has Cu-rich chemistry, while lighter phase along the inclusion periphery is enriched in O, Cr, Fe and Zn (Table 2, analyses 12 and 13). Some Cu-Ag-Au spherules contain faceted (crystalline) Cu-rich inclusions, which display cubic or hexagonal shapes in spherule cross-sections, as well as dendrite-like inclusions with irregular outlines. Individual spherules include rounded cavities encrusted with dendritic Cu-Ag-Au segregations (Figure 13f; Table 2).

Two gold-bearing spherules with bulk Cu-Ag-Au-Ni-Zn composition (Ni = 8.06 wt.%, Cu = 27.95 wt.%, Zn = 5.36 wt.%, Ag = 1.98 wt.%, Au = 56.65 wt.%) are characterized by well-developed exsolution texture (Figure 13i). Figure 13i illustrates the typical distribution of dendritic arrays (lamellae) within an individual spherule with «dark» and «grey» lamellae concentrating within the upper and central portions of the spherule and «white» lamellae concentrating within its lower part. Compositional differences between various lamellae are shown in Figure 14. Dark lamellae are slightly depleted in Au and Ag and enriched in Ni and Cu in reference to the average spherule composition (determined by EDS scanning of the entire cross-section through these spherules). Grey and white lamellae appear to be enriched in Au and depleted in Cu and Ni in comparison with the average spherule (Figure 14). Silver and zinc are slightly enriched in the grey lamellae and virtually absent in the white lamellae (Figure 14).

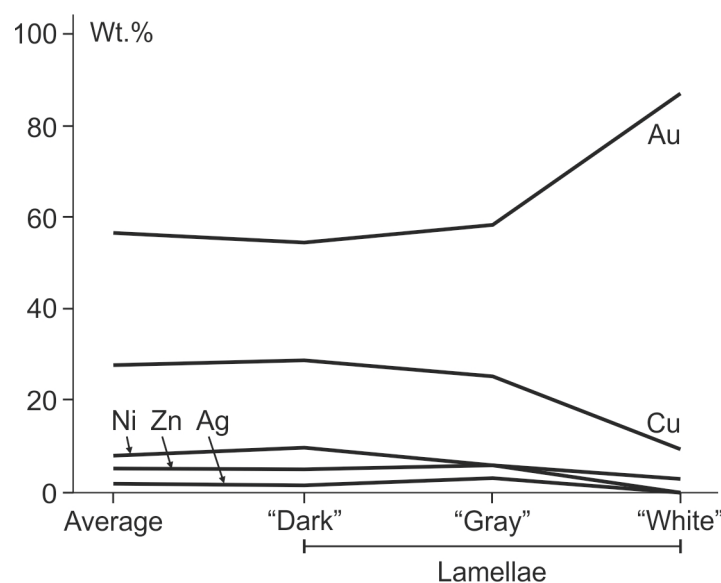


Figure 14. Compositional variations in various lamellae and their host Cu-Ag-Au-Ni-Zn spherules.

5.5. Gold in Pyroclastic Rocks from the Kaylan Deposit

Hematite-rich tuff from the Kaylan iron-oxide deposit contains a single irregular grain of Fe-Ni-Cu-Ag-Au composition (Figure 15a) and multiple (total of 10 grains recovered) Cu-Ag-Au spherules with typically deformed surfaces due to solidification and compaction during progressive cooling (Figure 15b–f). Two of the gold-bearing spherules are characterized by homogeneous internal structure (Figure 15b), while other Cu-Ag-Au spherules contain abundant Cu-rich inclusions, which are frequently grouped into spiral-shaped arrays and clusters chaotically distributed with the volume of individual spherules (Figure 15c). Copper-rich micro-inclusions (typically under 1 μm in size) in most cases display rounded shapes (Figure 15d) along with less common faceted (hexagonal and prismatic; Figure 15e) or dendritic (Figure 15f) outlines. Based on the EDS analyses, all micro-inclusions, independently of their shape and texture, are enriched in copper and oxygen in comparison with spherule matrices (Figure 15d–f) and contain minor zinc (0–4.2 wt.%) and iron (0–1.5 wt.%).

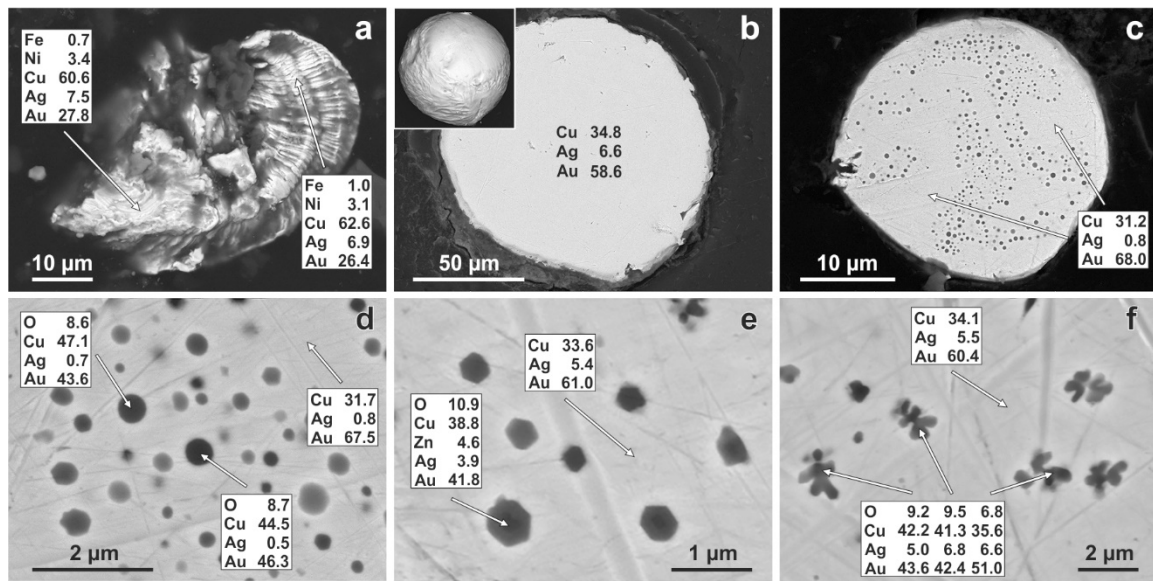


Figure 15. Shapeless gold-bearing particle (a) and spherules (b–f) in hematite-bearing tuff from the Kaylan deposit: (b)—homogeneous spherule; (c)—spherule with spiral-shaped arrays of Cu-rich inclusions; (d–e)—rounded (d), faceted (e) and dendritic (f) Cu-rich inclusions.

5.6. Some Experimental Considerations

To provide further constraints on possible origins of the Cu-Ag-Au spherules, we have carried melting experiments at atmospheric conditions using synthetic alloys with compositions (Cu₃₀Ag₁₅Au₅₅), which closely approximate chemistry of natural spherules determined by the SEM-EDS. Spherules ranging in size between 0.2–0.5 mm were formed under the propane burner flame (~1300 °C) in both presence and absence of the anti-oxidant flux (Na₂B₄O₇). The quenching of spherules was achieved through termination (several seconds) of propane burner application, or through dropping of molten spherule into cold water (fractions of a second). Results of these experiments are summarized in Figure 16.

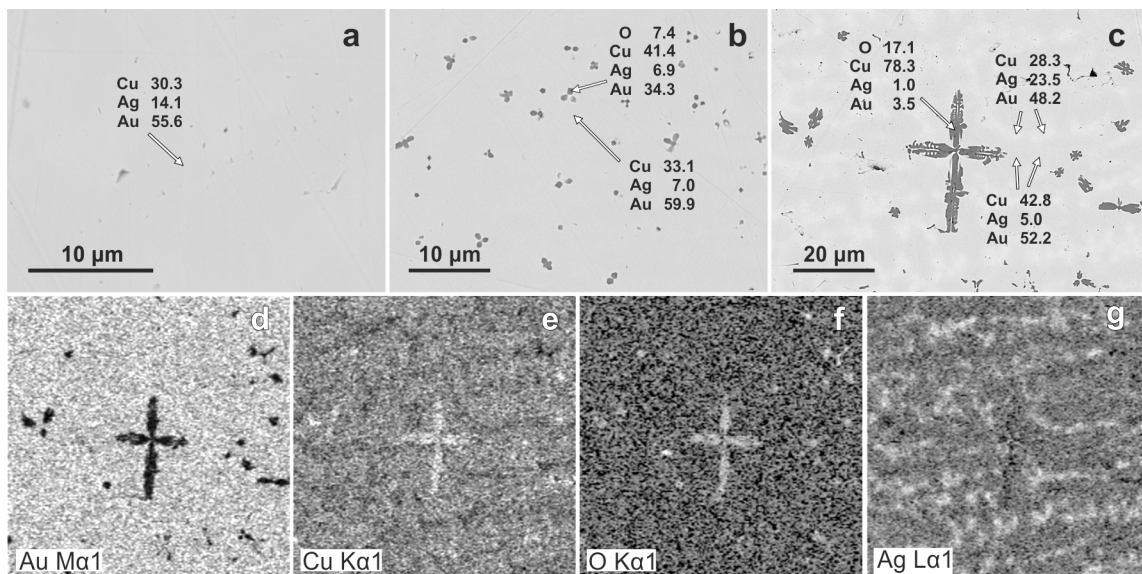


Figure 16. EDS images for Cu-Ag-Au spherules obtained in oxygen-free (a) and at atmospheric conditions (b,c) experimental runs with water quenching (a,b) and free air cooling (c); (d–g)—results of scanning of cross-section (c) in characteristic Au Mα1 (d), Cu Kα1 (e), O Kα1 (f) and Ag Lα1 (g) rays.

Our data indicate that oxygen-free melting and quenching results in the formation of compositionally homogeneous spherules (Figure 16a). At the same time, differences between actual analytical data points and composition of original Cu-Ag-Au mixture used in melting experiments suggests incipient chemical differentiation in quenched experimental spherules. Melting under atmospheric conditions followed by quenching in water leads to the formation of skeletal crystals enriched in Cu and O within experimentally produced spherules (Figure 16b). Increase in cooling time is coupled with the increase of the skeletal crystal size and further differentiation of the spherule matrix to the point of formation of alternating areas with different copper and silver contents (Figure 16c). Composition of skeletal crystals and matrix differentiates is well reflected in SEM images produced via scanning of the sample in characteristic Au, Cu, O and Ag radiation (Figure 16d–g). Copper to oxygen ratio based on numerous EDS analyses of the skeletal crystals ranges from 1 to 2 possibly reflecting variable oxygen fugacity values within different portions of experimental spherules.

It is important to mention that spherules obtained in experimental melting runs do not contain spherical Cu-O inclusions and meniscus-like textures (Figure 10e,h, Figure 11d,e, Figures 13f–h and 15c,d). This can possibly be explained by the difference in cooling processes between experimental runs and natural conditions, where relatively large ($3\text{--}50 \times 10^{-2} \text{ mm}^3$) synthetic spherules experience longer cooling times (under equal other conditions) in comparison with the smaller ($4\text{--}550 \times 10^{-6} \text{ mm}^3$) natural spherules. X-ray diffraction pattern of water-quenched synthetic spherules shows presence of Cu_3Au substitution solid solutions in the experimental run products (Figure 17). Characteristic broadening of diffraction peaks and non-stoichiometric compositions (closer to $\text{Cu}_{2.7}\text{Au}_1$) may indicate existence of imperfections (defects) in the crystal lattice of these intermetallic compounds.

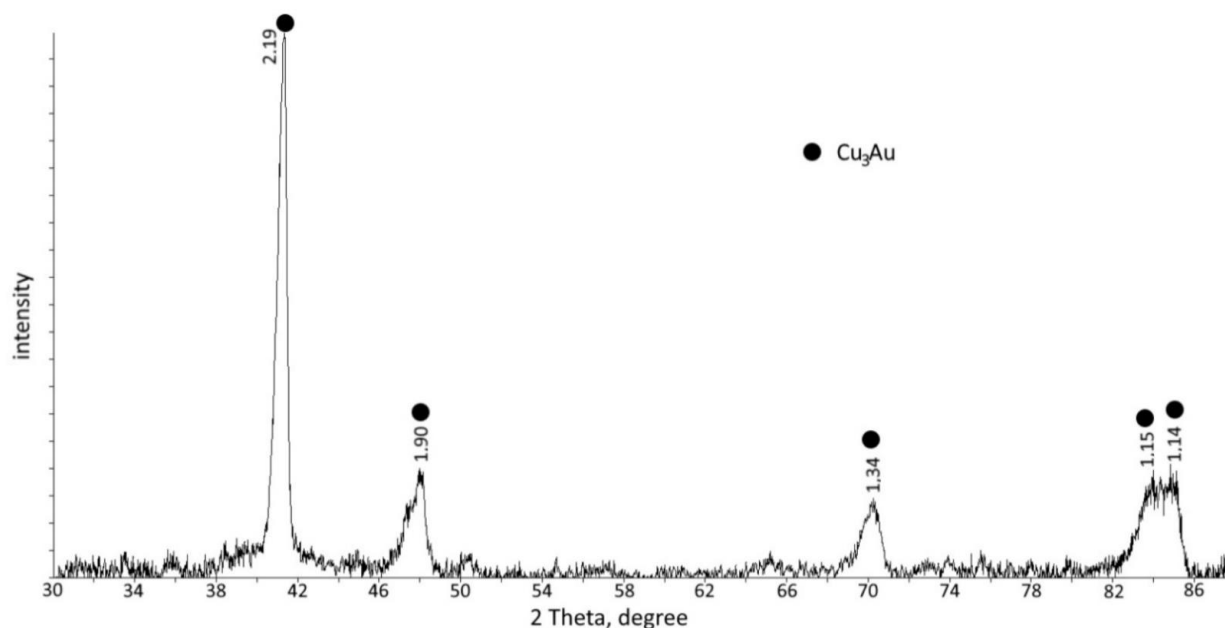


Figure 17. X-ray diffraction pattern of quenched (cold water) Cu-Ag-Au spherules obtained in experimental melting runs at atmospheric conditions (see text for details).

6. Discussion

6.1. Origin of Cu-Ag-Au Spherules

Most rocks in this study contain numerous Cu-Ag-Au intermetallic spherules. One exception includes iron-oxide ores and associated explosive breccias from the Poperechnoye deposit, which are dominated by almost copper-free gold-silver alloys (see discussion below). The spherical shape and common soft deformations of the most gold-bearing spherules suggest their formation in a volcanic melt or fluid. Based on the phase diagram

for the ternary Au-Cu-Ag system [77–79], gold-bearing spherules from the LKR ores and volcanic rocks were formed at temperatures of not less than 950 °C (Figure 18). Gold and silver form homogeneous alloys with copper within the temperature range characteristic of most high-temperature hydrothermal and magmatic processes [80,81]. Decrease of temperature in the molten Cu-Ag-Au alloys will trigger their solidification followed by the exsolution of solid phases with variable concentrations of Cu, Ag and Au [82]. As we do not observe Cu-, Ag- and Au-rich exsolution structures similar to [82] in our samples, we conclude that homogenous intermetallic spherules in the LKR deposits have experienced very fast cooling, possibly below the solidus temperature. Since Cu-Ag-Au alloys produced in our experiments and natural spherules share clear compositional similarities, we propose that the matrix of the latter is also dominated by Cu_3Au compositions.

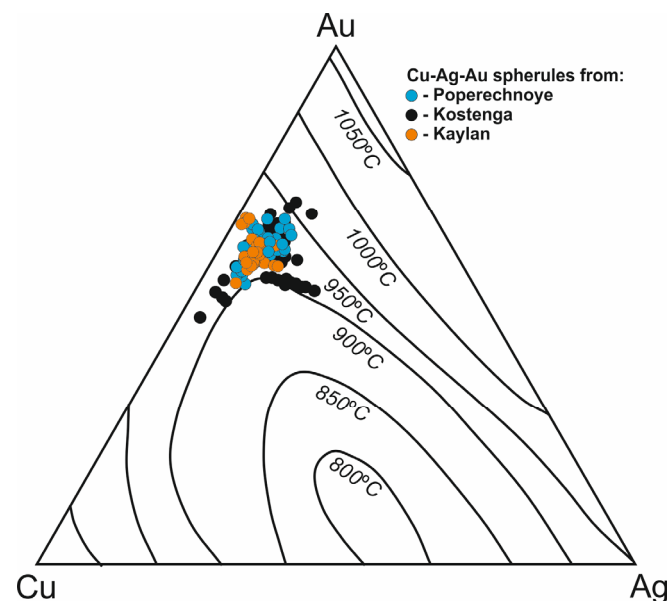


Figure 18. Compositions of Cu-Au-Ag spherules plotted on ternary phase diagram for Au-Cu-Ag modified after [77] with additions from [78,79]. Lines depict liquidus temperatures at different end-member compositions.

Temperature range characteristic of most high-temperature hydrothermal and magmatic processes [80,81]. Decrease of temperature in the molten Cu-Ag-Au alloys will trigger their solidification followed by the exsolution of solid phases with variable concentrations of Cu, Ag and Au [82]. As we do not observe Cu-, Ag- and Au-rich exsolution structures similar to [82] in our samples, we conclude that homogenous intermetallic spherules in the LKR deposits have experienced very fast cooling, possibly below the solidus temperature. Since Cu-Ag-Au alloys produced in our experiments and natural spherules share clear compositional similarities, we propose that the matrix of the latter is also dominated by Cu_3Au compositions.

6.2. Origin of Cu-O Micro-Inclusions in Gold-Bearing Spherules

Cu-Ag-Au spherules frequently contain spherical, dendritic or faceted Cu-O micro-inclusions (Figures 10, 11, 13 and 15). Globular shape of some Cu-O inclusions suggests their formation through liquid immiscibility. Gold and silver oxides are unstable at respective temperatures of 160 °C and 230 °C [78,79]. Consequently, gold and silver in Cu-Ag-Au alloys are completely dissolved in copper at temperatures above the liquidus and exhibit chemically inert behavior during formation of Cu- and O-rich phases (inclusions). This allows us to analyze this process using the phase diagram for the Cu-O system (Figure 19).

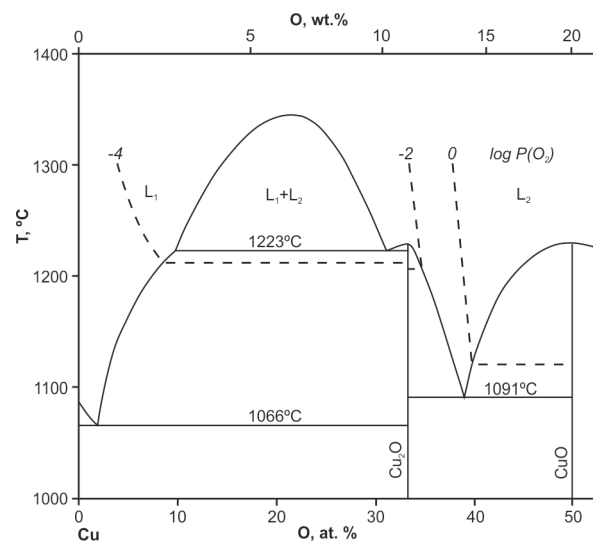


Figure 19. Phase diagram for the Cu-O system modified after [83]. Isobaric curves for $\log P(O_2)$ are shown by the dashed line.

The Cu-O diagram defines an area of splitting of primary copper melt into two immiscible liquids ($L_1 + L_2$) represented by conjugate copper-rich (L_1) and oxygen-rich (L_2) compositions (Figure 18). We suggest that in our samples, copper-rich melt L_1 represents the spherule matrix, while oxygen-rich melt L_2 is compositionally similar to Cu-O micro-inclusions. The Cu-O system below 1223 °C within this given compositional range will be represented by copper liquid in equilibrium with cuprite, with the latter being stable all the way to the room temperature. Our data (Table 2, analyses 10 and 11) suggest predominant copper-oxide composition of the micro-inclusions in Cu-Ag-Au spherules with an average atomic ratio of Cu/O of 3/2. At least a portion of oxygen analyzed by the EDS will be partitioned in iron oxides. Moreover, several studies indicate that the EDS analysis of metallic surfaces commonly overestimates oxygen concentrations by up to 3.8 wt.% [84–86]. Based on the above, we expect the Cu/O ratio in the spherule-hosted micro-inclusions to be even higher, which is consistent with the bulk cuprite (Cu_2O) compositions of the latter.

Formation of Cu-O inclusions requires that the cooling alloy contain sufficient amount of oxygen. This requirement is consistent with the results of our melting and fast cooling experiments with Cu-Ag-Au alloys. Melting and cooling of molten Cu-Ag-Au droplets in presence of the antioxidant flux ($Na_2B_4O_7$) indicate that no formation of copper oxide inclusions takes place under these conditions. The latter start to occur only during the flux-free cooling of molten Cu-Ag-Au droplets in air (Figure 16). According to the phase diagram for the system Cu-O (Figure 19), the immiscibility field $L_1 + L_2$ (responsible for the formation of initially liquid Cu_2O -enriched inclusions in Cu-Ag-Au spherules) correspond to $\log P(O_2)$ of around -3 . This value appears to be representative of oxygen fugacity during formation of the LKR ores and associated magmatic rocks.

Some larger copper oxide inclusions in Cu-Ag-Au spherules display presence of solidified meniscus-like textures (Figure 10e,h and Figure 13h), separating two phases with distinctly different chemical compositions (Table 2). This interesting petrologic phenomenon requires further detailed investigations. In the current study, we would like to preliminary propose that these textures may represent liquid immiscibility processes developing at several levels: (1) immiscibility related to separation of initially liquid Cu-Ag-Au spherules from a primary metal-silicate melt; (2) formation of immiscible copper-oxide inclusions in molten Cu-Ag-Au spherules and, finally, (3) separation of molten copper-oxide globules into two conjugate liquids with contrasting chemical compositions. According to [87,88], such “multi-immiscibility” processes may occur only under conditions of extremely fast cooling (super-cooling) of metallic melts (not less than 100–200 K/s [89]), which may lead to the formation of metastable alloys.

Copper oxide inclusions in Cu-Ag-Au spherules from the LKR iron oxide deposits mostly display spherical (Figure 11d,e, Figures 13f–h and 15d), dendritic (Figures 11f, 13h and 15f) or faceted (Figure 15e) shapes. All three types may also co-exist in a single sample and within one cross-section of the individual intermetallic spherule (Figure 13h). Cuprite melt in case of spherical inclusions have solidified without visible crystallization (formation of initial crystallites). Dendritic inclusions record initial stages of crystallization of a copper-oxide liquid, while faceted inclusions are developed in case of the protracted crystallization of primary copper-oxide melt trapped in Cu-Ag-Au spherules. Crystallization temperature for cuprite is estimated at 1242 °C [90]. Apparently, this temperature is characteristic of cooling processes involving Cu-Ag-Au spherules above their liquidus temperature of ~950 °C (Figure 18). Differences in the degree of crystallinity of copper-oxide micro-inclusions (e.g., evolution from spherical to dendritic to faceted shapes) are most probably related to their cooling rates. Extremely fast cooling leads to the formation of homogeneous spherical inclusions, while slower cooling rates result in dendritic or faceted crystalline forms. It is worth to mention that no spherical inclusions or meniscus-like textures were produced in our experimental runs; all cuprite inclusions display clear skeletal crystalline shapes (Figure 16a–c). We tend to explain this discrepancy by intrinsic differences between volumes (mass) of studied spherules in both cases. Synthetic spherules typically have larger volumes ($3\text{--}50 \times 10^{-2} \text{ mm}^3$) resulting in slower cooling gradients, while smaller individual volumes of natural spherules ($4\text{--}550 \times 10^{-6} \text{ mm}^3$) trigger much faster cooling (quenching) conditions.

6.3. Origin of Ni-Cu-Zn-Ag-Au Spherules

Rare Ni-Cu-Zn-Ag-Au spherules from the Kostenga iron-oxide ore (Figure 13i) are characterized by high-temperature metastable state of the intermetallic alloy. Ni- and Zn-enriched compounds of this alloy are lacking any textural evidence for the incipient crystallization centers as well as for the expansion and continuation of crystal growth within an individual metallic spherule. Ni-Cu-Zn-Ag-Au spherules are characterized by fuzzy boundaries between compositionally similar areas as well as by presence of isolated areas with elevated gold concentrations consistent with abrupt termination of metal diffusion processes. This, in our opinion, is best explained by fast cooling of metal droplets. Under equilibrium conditions, based on the chemical composition of these spherules, progressive cooling would have resulted in the formation of dendritic [91,92], granular [93], or lamellar [82] spherule textures.

6.4. Origin of Ti-Cu-Ag-Au Intermetallic Compounds in Association with Baddeleyite

Among the total of nine grains of intermetallic Ti-Cu-Ag-Au compound extracted from the LKR rocks, six grains are associated with baddeleyite (Figure 13c) and, in some cases, with zircon and quartz. Formation temperatures for zircon-quartz-baddeleyite mineralization from the Algama deposit (Khabarovsk region of the Russian Far East), determined using fluid inclusions in ore minerals, range from 110° to 370 °C [94]. Korzhinskaya et al. [95] demonstrated stability of the association $\text{ZrSiO}_4\text{-SiO}_2\text{-ZrO}_2$ in alkaline solutions at temperature of 500 °C and pressure of 1 kbar. Grains of intermetallic Ti-Cu-Ag-Au are composed predominantly of two major constituents: a) matrix (copper-based solid solution with compositions close to $\text{Al}_5\text{Ti}_1\text{Cu}_{76}\text{Zn}_3\text{Ag}_6\text{Au}_9$; Here and elsewhere chemical formula coefficients are calculated on the oxygen-free basis using the SEM-EDS analyses (atomic%)), which occupies on average 64% of the internal structure of individual grains and b) network of titanium- and gold-enriched inclusions, which occupy the remaining 36% of a typical cross-section through the Ti-Cu-Ag-Au grains (Figure 13c). Ti-bearing inclusions display complex internal structure under higher magnification (Figure 13d). These inclusions are characterized by the gradual transition from Au-rich, $\text{Ti}_{31}\text{Cu}_{32}\text{Ag}_1\text{Au}_{36}$ phase in the center of the inclusion (analysis 2 in Figure 13d) to the $\text{Ti}_{30}\text{Cu}_{26}\text{Ag}_1\text{Au}_{43}$ phase with higher levels of Au enrichment (analysis 3 in Figure 13d) and, finally, to the Ag-rich, $\text{Cu}_{12}\text{Zn}_3\text{Ag}_{73}\text{Cd}_5\text{Au}_6$ compositional rim of the zoned intermetallic Ti-Cu-Ag-Au (with Zn

and Cd) compound (analysis 4 in Figure 13d). In addition, the matrix of Ti-Cu-Ag-Au grains contains phases with compositions approaching $Al_4Ti_{65}Cu_{12}Ag_2Au_{17}$, which are not texturally associated with Au-rich micro-inclusions (analysis 5 in Figure 13d).

Intermetallic Ti-Cu-Ag-Au and Ti-Cu-Au systems commonly display rather complex phase structure and thermodynamic behavior [96,97]. In the Ti-Ag binary system at temperatures below 1000 °C, formation of Ti_2Ag and Ti-Ag is permitted and possible, while Ti_3Au , TiAu, $TiAu_2$, $TiAu_6$ alloys are formed in the Ti-Au binary system under 960 °C and Ti_2Cu , TiCu, Ti_3Cu_4 , Ti_2Cu_3 , $TiCu_2$ and $TiCu_4$ compounds form in the Ti-Cu compositional space at the temperatures below 1495 °C [98]. Based on these thermodynamic considerations, we propose that the intermetallic solid solution with several Ti-bearing phases crystallized in the range of 960 to 1495 °C. Ti-enriched phases in the matrix (analysis 5 in Figure 13d) are probably best approximated by titanium oxide composition.

Therefore, we conclude here that Ti-Cu-Ag-Au intermetallic grains were formed under high-temperature (>960 °C) conditions. Their average composition, normalized to the sum of Cu + Ag + Au + Ti, corresponds to $Ti_{13}Cu_{53}Ag_5Au_{29}$ composition and is similar to the general compositional range of Cu-Ag-Au spherules ($Cu_{54}Ag_{16}Au_{30}$), where silver is substituted for titanium. Based on these chemical comparisons, we suggest that Cu-Ag-Au spherules and Ti-Cu-Ag-Au intermetallic compounds were formed via the same petrologic processes, but, most probably, at different titanium concentrations. Textural differences (spherical versus irregular shapes) can be explained by the molten state of the spherules and solid state of Ti-alloys within the range of temperatures established in this study (960–1495 °C). Under this scenario, the lower-temperature baddeleyite-zircon-quartz assemblage in association with the Ti-bearing intermetallides was formed at a later stage, most probably during hydrothermal-metasomatic (skarn-related) re-organization of primary gold alloy-bearing volcanic rocks.

6.5. Origin of Ag-Au Alloys

Gold-silver alloys were recovered from all types of ores and associated volcanic rocks from the LKR iron oxide deposits with an exception of Poperechnoye carbonatite-like rocks and Kaylan Fe-Mn mineralization (Figure 8). Au-Ag grains are typically compositionally homogeneous and their gold fineness (650–1000‰) is comparable with fine gold from peridotites in the Ospinsky-Kitoysky massif (Buryatia), Talnakh and Oktyabrsky sulfide deposits in Norilsk, Berezovy mineralization in the Urals, Batu-Hijau gold-copper system in Indonesia, Kondyor alluvial mineralization (Khabarovsk region) and ultramafic-mafic rocks of the Khurai-Zhalginsky massif in the East Sayan Mountains [81]. In all the cases mentioned above, gold is crystalline in nature and its formation is attributed to the late- and post-magmatic stages of the evolution of ultramafic-mafic magma [81]. We suggest that Ag-Au alloys from the LKR ore province were formed through the hydrothermal alteration of gold-bearing volcanic (especially pyroclastic) rocks. This is consistent with occurrence of Ag-Au grains that are syngenetic with the hydrothermal iron-oxide mineralization at the Poperechny deposit (Figure 9d,e). The lack of Ag-Au grains in carbonatite-like rocks from the Poperechny and iron oxide ores from the Kaylan deposits can be possibly explained by weak hydrothermal alteration of these formations. We propose that the LKR volcanic rocks and iron-oxide ores contain at least two generations of gold mineralization: 1) the early magmatic Cu-Ag-Au spherules and 2) the later-stage hydrothermal Ag-Au grains.

6.6. Formation of Au-Bearing Compounds in Mineralized Volcanic Systems

The data presented above suggest an initially magmatic origin for gold-bearing alloys in iron-oxide ore and associated volcanic rocks from the LKR deposits and emphasizes role of liquid immiscibility processes in precious metal evolution in mineralized volcanic systems. However, possible trigger mechanisms and conditions necessary for separation of precious metal phases from silicate, sulfide and sulfide-silicate melts still remain quite enigmatic [16,35,38,39,44,48,49,52]. Previous studies suggest that gold crystallizes from silicate melt as native element or intermetallic compound (typically with copper and

silver) [14–17,39,47,48,99], or as a minor component in base metal sulfides [100–103]. In subduction-related environments, gold is preferentially partitioned into sulfide (monosulfide solid solution, or MSS) phase, especially under oxidized and sulfur-rich conditions [28,31,32,49–56,58]. Other factors contributing to either gold concentration or fractionation in magmatic environment include pressure and salinity of melts and associated fluids [104–107]. For example, gradual decrease in pressure in crustal magma conduits will result in sulfide decomposition and partitioning of gold into the silicate liquid [106]. At shallow levels, in sub-volcanic environment, other factors such as redox conditions may play the most important role in determining overall gold budgets in mineralized volcanic systems [108–113]. Moreover, addition of ~3000–4000 ppm (0.3–0.4 wt.%) of chlorine to the hydrous andesite melt increases solubility of gold by a factor of 1.5 in comparison to Cl-poor melts [105]. Below we briefly review current petrologic models explaining behavior of gold in evolving (through fractional crystallization, liquid immiscibility and fluid-triggered transport) magmatic systems with variable sulfur activity.

The behavior of gold (as well as copper and silver) during magmatic differentiation of silicate magmas appears to be strongly controlled by sulfur content of these magmas [51–53,58,102]. In S-poor melts, gold is either preferentially sequestered (most probably as micro- and nano-nuggets [114,115]) along with platinum-group metals into fractionating silicate liquids or the early-stage crystalline mush below the top of convective, differentiating magma chamber [116]. Experimental data suggest that gold-bearing compounds (compositionally similar to Cu-Ag-Au alloys from the Lesser Khingan sites) can precipitate directly from silicate magma, typically as “nano-nuggets” (sub-micrometer phases) in the absence of any significant sulfide component [107,115,117]. Under this “gold nano-nugget crystallization” model, Cu-Ag-Au grains may have formed through direct crystallization of noble metals and copper from S-poor silicate melt under low-sulfur activity conditions. Under certain conditions in explosive systems, the Cu-Ag-Au alloys may become immiscible with the host silicate melt and form droplet-shaped micro-spherules. This model is consistent with the established formation conditions for the LKR deposits that lack any substantial primary sulfide mineralization, or sulfides observed in some samples are clearly of the later-stage hydrothermal origin.

Another way of forming gold-bearing alloys is through the desulphurization of primary magmatic sulfides enriched in noble and chalcophile metals. Noble metals are partitioned into base metal sulfides that crystallize from sulfide-rich silicate melts under wide range of pressures, temperatures, and sulfur and oxygen fugacity values [49–55,58,99–103]. Gold, in particular, exhibits chalcophile behavior during partial melting and magmatic crystallization and is strongly affected by presence or absence of sulfide phases during these processes [16,30–33,51–53]. Since sulfides are common minerals both in the mantle [31–33,118–120] and in various primitive and evolved silicate melts [51,102,121–124], gold is effectively scavenged by sulfide liquids during the course of magmatic evolution [16,49,53,55,116,122]. Further liberation of gold and formation of native gold particles or gold-bearing intermetallic compounds may follow several different scenarios.

Lawley and co-authors proposed that base metal sulfides also carrying substantial quantities of gold and platinum-group elements (PGE) become unstable during serpentinization of sulfide-bearing ultramafic rocks [125]. Under this scenario, Au, Ag, Pt and Pd partition into intermetallic compounds, when sulfides are replaced by metal alloys and native metals during serpentinization [125]. Co-existing base metal sulfides (chalcopyrite, bornite, pentlandite) and gold-bearing alloys (as well as native gold in some cases) have been reported from peridotites [28,126,127] and subduction-related ultramafic rocks [38,39,128]. These findings suggest that such serpentinization process accompanied by sulfide breakdown is operational in mantle-derived peridotites. However, the LKR volcanic systems and related noble metals mineralization were developed and emplaced under crustal conditions and are essentially of basaltic to dacitic bulk composition [59–61]. These rocks never experienced any serpentinization ([61], this study) and it is highly unlikely (based on bulk chemistry and petrology of the systems under consideration) that observed

Au-bearing spherules and intermetallic compounds in the LKR rocks were formed via sulfide replacement by native metals and noble metal alloys.

Large array of experimental data complemented by detailed studies of natural samples suggest that noble metals (Au, Ag and PGE) are preferentially partitioned into sulfides during crystallization of terrestrial magma [50–53]. In some cases (Norilsk), Au and Ag form Au-Cu and Au-Ag alloys in Cu-sulfides [129], while detailed studies indicate presence of PGE-Au nanoparticles in mineralized, sulfide-bearing horizons within the Merensky Reef of Bushveld Complex in South Africa [114]. Recent experiments suggest that the formation of noble metal nanoclusters and nanoparticles may precede large-scale sulfide crystallization of sulfur-rich silicate melts [130]. Reduction (desulfurization) of these Au, Ag and PGE-bearing Fe-Cu-Ni sulfides can potentially liberate noble metals as either native metals or intermetallic (Cu-Ag-Au) compounds [131]. Peregoedova and co-authors listed four possible mechanisms of sulfide desulfurization based on their experimental studies as well as natural examples [131]: (1) desulfurization may be triggered by pressure drop during crustal differentiation of mantle-derived, sulfide-rich magma, (2) excessive sulfides can be removed from Au-enriched sulfide mineralization by S-poor (under-saturated) melts or fluids, (3) reduction occurs during degassing of early-stage sulfide droplets in a sub-volcanic magma chamber and (4) sulfur can be potentially removed during interaction of sulfide with chromite in hypothetical magmatic conduit. Magma chamber degassing model is potentially applicable to the LKR situation on general geologic grounds (widespread occurrence of explosive volcanic rocks, evidence for magmatic differentiation, etc.). However, all proposed reduction mechanisms do not completely eliminate sulfide signature of noble metal-bearing melts and, based on experimental data, this desulfurization is only partial [131]. Absence of magmatic sulfides in the LKR volcanics argues against desulfurization of noble metal-bearing sulfides as a viable mechanism for the formation of the LKR Cu-Ag-Au alloys. We conclude that crystallization of Au-bearing compounds from metal-rich silicate melts accompanied by local metal-silicate liquid immiscibility was most probably responsible for the formation of precious metal mineralization associated with the LKR mineralized volcanic systems.

6.7. Possible Metallogenic Implications

As we attempted to show in the previous sections of this paper, textural and compositional features of gold-bearing alloys in the LKR iron-oxide ores and associated magmatic rocks are consistent with their origin through liquid immiscibility processes in the silicate-metallic liquid system with further dispersion of the gold-bearing particles through the evolving sub-volcanic plumbing system. Fast cooling features documented in many metallic micro-spherules could have been caused by injection of highly mobile fluid-saturated, spherule-bearing melt into upper crustal gashes, cavities and cracks during its progressive movement to the surface, or generated during the process of sub-aerial, sub-glacial or sub-marine eruption. The association of the LKR Cu-Ag-Au alloys with large-scale iron-oxide mineralization indicates possible involvement of silicate-metallic immiscibility and explosive volcanism in the formation of iron-oxide gold-copper (IOCG) deposits of the Andean type and related (by depth?) copper-gold porphyry systems as well as the deeper parts of sub-volcanic epithermal environments.

The IOCG deposits are characterized by distinctive magnetite and/or hematite enrichment [132] and, in case of the Andean Iron Belt, are spatially and temporally associated with prolific arc-related tholeiite and calc-alkaline plutonism of gabbroic to dioritic composition [133,134]. Andean iron oxide gold-copper deposits were formed mainly by magmatic-hydrothermal processes related to the emplacement and evolution of crustal plutonic complexes with additional (although, rather moderate) contribution from the accreted basement terranes and host volcanic rocks [134–136]. Besides volumetrically dominant iron oxides, IOCG-type mineralization includes copper sulfides (chalcopyrite, bornite), pyrite and gold [137]. Re-Os concentrations and initial Os isotope ratios in Andean IOCG are similar to those for Andean Cu-Au deposits suggest that both styles of this subduction-

related mineralization were formed by similar magmatic-hydrothermal processes and their relevant metal inventories were derived from comparable crustal sources in the Central Andes [136]. This conclusion is further supported by the Fe-O isotope systematics in the Mantoverde IOCG deposit in Chile [138]. Additional geologic (association with evaporitic minerals, such as phosphates; correlation with arid belts or evaporate-bearing basins; voluminous sodic alteration) and geochemical (presence of marialitic scapolite; fluid inclusions with salinities over 20 wt.% NaCl; isotopically heavy sulfur with $\delta^{34}\text{S} > 5\text{‰}$; low $\delta^{18}\text{O}$; radiogenic isotope ratios consistent with recycled meteoric waters) data also suggests involvement of regional basinal, non-magmatic fluids in the IOCG genesis [139–141].

Several studies suggested that both IOCG and gold-copper porphyry deposits are associated with potassic oxidized intermediate to felsic granitoids but differ in age, alteration styles, fluid compositions and ore mineralogy [142–145]. Fundamentally, IOCG are sulfur-poor and Precambrian in age, while porphyry deposits are sulfur-rich and occur in Phanerozoic subduction-related terranes [9,134,135,144,145]. The two Cu-Au-bearing systems are also characterized by contrasting fluid compositions: predominantly magmatic-hydrothermal $\text{H}_2\text{O}-\text{CO}_2-\text{NaCl}$ fluid with contributions from other (evaporitic, basinal, etc.) fluid sources in case of IOCG [134,139–142,146] and high salinity brines with significant vapor phase typical of Cu-Au porphyry systems [5,6,142,147–149]. Numerous studies suggest that gold in typical porphyry environment is transported in Cu-Fe-S-rich hydrothermal fluids [42,53,147,149,150] and deposited as small particles of native gold along the boundaries of bornite grains, or included as minor component (0.1–20 ppm) in sulfide phases [151]. Magmatic gold occurrence in the LKR ores and associated volcanic rocks suggests that primary magmatic forms can be introduced into a sub-volcanic environment and preserved in mineralized volcanic systems through fast cooling and quenching during explosive volcanic eruption. Our data also may indicate that gold in subduction-related environments crystallizes from metal-enriched silicate melts predominantly in the form of Cu-Ag-Au intermetallic compounds. Presence of liquid immiscibility phenomena (meniscus-like boundaries between different phases in some Cu-Ag-Au spherules) suggest that multi-level immiscibility processes could have taken place during evolution of the mineralized sub-volcanic conduits. Finally, our data point to possible existence of evolutionary forms in the magmatic-hydrothermal environments from Cu-Ag-Au alloys observed in (possibly deeper) IOCG-like systems to almost pure gold or gold-silver particles typical of common porphyry and epithermal environments. We may conclude that the formation of gold alloys in crustal magmatic plumbing systems (deep roots of arc volcanoes) may serve as a precursor (and also as an exploration guide) for high-grade epithermal gold mineralization at shallow structural levels of subduction-related hydrothermal-volcanic environments.

7. Concluding Remarks

Textural and compositional features of gold (Cu-Ag-Au, Ni-Cu-Zn-Ag-Au, Ti-Cu-Ag-Au, Ag-Au) alloys from iron oxide deposits in the Lesser Khingan Range (LKR) of the Russian Far East suggest their precipitation from evolving metal-rich silicate melts within the roots of volcanic mineralized systems. Hydrothermal processes that follow formation of magmatic gold assemblages resulted in redistribution, purification and concentration of gold that may lead to the formation of epithermal and porphyry deposits in magmatic arcs and accretionary orogens.

Emergence of magmatic gold alloys in the LKR iron deposits appears to be triggered by high concentrations of gold, silver and copper in primary silicate melts. Gold spherules were formed through silicate-metal liquid immiscibility and then injected into fissures surrounding the ascending melt column, or emplaced through a volcanic eruption. Presence of globular (occasionally with meniscus-like textures) Cu-O micro-inclusions in Cu-Ag-Au spherules suggests their crystallization under extremely fast cooling conditions. Irregularly shaped Cu-Ag-Au particles were formed through hydrothermal alteration of gold-bearing volcanic rocks and ores. We propose that slow cooling in the evolving melt conduits will lead to deformation of primary gold spherules during the magmatic mineral growth and

formation of irregularly shaped Cu-Ag-Au particles observed in some subduction-related plutonic complexes [39].

Presence of Cu-Ag-Au spherules in a wide range of igneous formations (explosive volcanic breccias and tuffs, basaltic intrusions, carbonatite-like and ultramafic rocks) along with their relatively constant chemical composition (restricted variations of the Cu:Ag:Au ratio in gold alloys from all above mentioned rock types), suggest that Cu-Ag-Au alloys may represent a universal textural and compositional manifestation of gold during early stages of evolution of mineralized magmatic-hydrothermal systems.

The association of the LKR Cu-Ag-Au alloys with large-scale iron-oxide mineralization indicates possible involvement of silicate-metallic immiscibility and explosive volcanism in the formation of the Andean-type IOCG and copper-gold porphyry deposits. We propose that gold mineralization in magmatic-hydrothermal systems evolves from Cu-Ag-Au alloys observed in deeper IOCG-type systems to almost pure gold or gold-silver particles typical of porphyry and epithermal environments.

Author Contributions: Conceptualization, N.B. and P.K.; field work, N.B. and V.N.; methodology, N.B., V.N. and I.A.; formal analysis, N.B., V.N., P.K. and I.A.; investigation, N.B., V.N., P.K., I.A. and N.K.; resources, N.B., V.N., I.A. and N.K.; data curation, N.B., V.N. and I.A.; writing—original draft, N.B. and P.K.; writing—review and editing, N.B., V.N. and P.K.; supervision—N.B.; project administration—N.B.; funding acquisition—N.B. and V.N. All authors have read and agreed to the published version of the manuscript.

Funding: This work was carried out within the State Assignment for the Institute of Tectonics and Geophysics, Far East Branch of Russian Academy of Sciences, Khabarovsk, Russian Federation.

Institutional Review Board Statement: Not applicable.

Informed Consent Statement: Not applicable.

Data Availability Statement: The data presented in this study are available within this article.

Acknowledgments: A.I. Bukhanchenko and N.M. Zvereva of the DV TFGU (Regional Fund of Geological Information, Khabarovsk, Russian Federation) are greatly acknowledged for providing invaluable information and samples from previous exploration on the LKR iron oxide deposits. I.G. Tsoi, A.V. Shtareva and L.M. Ilyin are thanked for their kind support of the analytical work (bulk chemical analyses of rocks and ores) at the Kosygin Institute of Tectonics and Geophysics (Khabarovsk, Russian Federation). The Academic Editor of Geosciences and three anonymous referees are also thanked for their contribution to improve the first version of the manuscript. This paper benefited from fruitful discussions with Nikita Kepezhinskas (University of Alberta, Edmonton, Canada). A.G. Molchanov is thanked for help during field work in the Lesser Khingan Range and field photographs.

Conflicts of Interest: The authors declare no conflict of interest.

References

1. Anoshin, G.N.; Kepezhinskas, V.V. Petrochemical features related to gold distribution for the Cenozoic volcanic rocks of the Kuril-Kamchatka province. *Geochem. Int.* **1972**, *9*, 618–629.
2. Mitchell, A.H.; Bell, J.D. Island arc evolution and related mineral deposits. *J. Geol.* **1973**, *81*, 381–405. [[CrossRef](#)]
3. Sillitoe, R.H.; Bonham, H.F., Jr. Volcanic landforms and ore deposits. *Econ. Geol.* **1984**, *79*, 1286–1298. [[CrossRef](#)]
4. Berger, B.R.; Bonham, H.F., Jr. Epithermal gold-silver deposits in the western United States: Time-space products of evolving plutonic, volcanic and tectonic environments. *J. Geochem. Explor.* **1990**, *36*, 103–142. [[CrossRef](#)]
5. Hedenquist, J.W.; Lowenstern, J.B. The role of magmas in the formation of hydrothermal gold deposits. *Nature* **1994**, *370*, 519–527. [[CrossRef](#)]
6. Audetat, A.; Gunther, D.; Heinrich, C.A. Formation of a magmatic-hydrothermal deposit: Insights with LA-ICP-MS. *Science* **1998**, *279*, 2091–2094. [[PubMed](#)]
7. Simon, G.; Kesler, S.E.; Russell, N.; Hall, C.M.; Bell, A.; Pinero, E. Epithermal gold mineralization in an old volcanic arc: The Jacinto Deposit, Camaguey District, Cuba. *Econ. Geol.* **1999**, *94*, 487–506. [[CrossRef](#)]
8. Defant, M.J.; Kepezhinskas, P. Evidence suggests slab melting in arc magmas. *EOS, Trans. Amer. Geophys. Union* **2001**, *82*, 65–69. [[CrossRef](#)]

9. Mungall, J.E. Roasting the mantle: Slab melting and the genesis of major Au and Au-rich Cu deposits. *Geology* **2002**, *30*, 915–918. [[CrossRef](#)]
10. Simon, A.C.; Pettke, T.; Candela, P. Experimental determination of Au solubility in rhyolite melt and magnetite: Constraints on magmatic Au budgets. *Amer. Mineral.* **2003**, *88*, 1644–1651. [[CrossRef](#)]
11. Richards, J.P.; Kerrich, R. Adakite-like rocks: Their diverse origins and questionable role in metallogenesis. *Econ. Geol.* **2007**, *102*, 537–576. [[CrossRef](#)]
12. Longo, A.A.; Dilles, J.H.; Grunder, A.L.; Duncan, R. Evolution of calc-alkaline volcanism and associated hydrothermal gold deposits at Yanacocha, Peru. *Econ. Geol.* **2010**, *105*, 1191–1241. [[CrossRef](#)]
13. Goff, F.; Stimac, J.A.; Larocque, A.C.L.; Hulen, J.B.; McMurtry, G.M.; Adams, A.B.; Roldan, M.A.; Trujillo, N.P.E., Jr.; Counce, D.; Chipera, S.J.; et al. Gold degassing and deposition at Galeras volcano, Colombia. *GSA Today* **1994**, *4*, 243–247.
14. Sisson, T.W. Native gold in a Hawaiian alkaline magma. *Econ. Geol.* **2003**, *98*, 643–648. [[CrossRef](#)]
15. Zhang, Z.; Mao, J.; Wang, F.; Pirajno, F. Native gold and native copper grains enclosed by olivine phenocrysts in a picrite lava of the Emeishan large igneous province, SW China. *Amer. Mineral.* **2006**, *98*, 643–648. [[CrossRef](#)]
16. Zelenski, M.; Kamenetsky, V.S.; Hedenquist, J. Gold recycling and enrichment beneath volcanoes: A case study of Tolbachik, Kamchatka. *Earth Planet. Sci. Lett.* **2016**, *437*, 35–46. [[CrossRef](#)]
17. Li, P.; Boudreau, A.E. Vapor transport of silver and gold in basaltic lava flows. *Geology* **2019**, *47*, 877–880. [[CrossRef](#)]
18. Fulignati, P.; Sbrana, A. Presence of native gold and tellurium in the active high-sulfidation hydrothermal system of the La Fossa volcano (Vulcano, Italy). *J. Volcanol. Geotherm. Res.* **1998**, *86*, 187–198. [[CrossRef](#)]
19. Henley, R.W.; Berger, B.R. Nature's refineries—metals and metalloids in arc volcanoes. *Earth-Sci. Rev.* **2013**, *125*, 146–170. [[CrossRef](#)]
20. Taran, Y.A.; Bernard, A.; Gavilanes, J.C.; Africano, F. Native gold in mineral precipitates from high-temperature volcanic gases of Colima Volcano, Mexico. *Appl. Geochem.* **2002**, *15*, 337–346.
21. Chaplygin, I.; Yudovskaya, M.; Vergasova, L.; Mokhov, A. Native gold from volcanic gases at Tolbachik 1975–76 and 2012–13 Fissure Eruptions, Kamchatka. *J. Volcanol. Geotherm. Res.* **2015**, *307*, 200–209. [[CrossRef](#)]
22. Simmons, S.F.; Brown, K.L.; Browne, P.R.L.; Rowland, J.V. Gold and silver resources in Taupo Volcanic Zone geothermal systems. *Geothermics* **2016**, *59*, 205–214. [[CrossRef](#)]
23. Shevko, E.P.; Bortnikova, S.B.; Abrosimova, N.A.; Kamenetsky, V.S.; Bortnikova, S.P.; Panin, G.L.; Zelenski, M. Trace elements and minerals in fumarolic sulfur: The case of Ebeko volcano, Kuriles. *Geofluids* **2018**, *2018*, 6363. [[CrossRef](#)]
24. Edmonds, M.; Mather, T.A.; Liu, E.J. A distinct metal fingerprint in arc volcanic emissions. *Nat. Geosci.* **2018**, *11*, 790–794. [[CrossRef](#)]
25. Zoller, W.H.; Parrington, J.R.; Kotra, P.J.M. Iridium enrichment in airborne particles from Kilauea volcano: January. *Science* **1983**, *222*, 1118–1121. [[CrossRef](#)] [[PubMed](#)]
26. Meeker, G.; Chuan, R.L.; Kyle, P.R.; Palais, J. Emission of elemental gold particles from Mount Erebus, Ross Island, Antarctica. *Geophys. Res. Lett.* **1991**, *18*, 1405–1408. [[CrossRef](#)]
27. Zelenski, M.; Kamenetsky, V.S.; Taran, Y.; Kovalskii, A.M. Mineralogy and origin of aerosol from an arc basaltic eruption: Case study of Tolbachik Volcano, Kamchatka. *Geochem. Geophys. Geosys.* **2020**, *21*. [[CrossRef](#)]
28. Leblanc, M. Co-Ni arsenide deposits, with accessory gold, in ultramafic rocks from Morocco. *Can. J. Earth Sci.* **1986**, *23*, 1592–1602. [[CrossRef](#)]
29. Kogiso, T.; Suzuki, T.; Shinotsuka, K.; Uesugi, K.; Takeuchi, A.; Suzuki, Y. Detecting micrometer-scale platinum-group minerals in mantle peridotite with microbeam synchrotron radiation X-ray fluorescence analysis. *Geochem. Geophys. Geosys.* **2008**, *9*. [[CrossRef](#)]
30. Tassara, S.; Gonzalez-Jimenez, J.M.; Reich, M.; Schilling, M.E.; Morata, D.; Begg, G.; Saunders, E.; Griffin, W.L.; O'Reilly, S.Y.; Gregoire, M.; et al. Plume-subduction interaction forms large auriferous provinces. *Nat. Commun.* **2017**, *8*. [[CrossRef](#)]
31. Lorand, J.P.; Keays, R.R.; Bodinier, J.L. Copper- and noble metal enrichment across the asthenosphere-lithosphere mantle diapirs: The Lanzo lherzolite massif. *J. Petrol.* **1993**, *34*, 1111–1140. [[CrossRef](#)]
32. Lorand, J.P.; Pattou, L.; Gros, M. Fractionation of platinum-group elements and gold in the upper mantle: A detailed study in Pyrenean orogenic lherzolites. *J. Petrol.* **1999**, *40*, 957–981. [[CrossRef](#)]
33. Kepezhinskas, P.; Defant, M.J.; Widom, E. Abundance and distribution of PGE and Au in the island-arc mantle: Implications for sub-arc metasomatism. *Lithos* **2002**, *60*, 113–128. [[CrossRef](#)]
34. Saunders, J.E.; Pearson, N.J.; Reilly, O.S.Y.; Griffin, W.L. Gold in the mantle: A global assessment of abundance and redistribution processes. *Lithos* **2018**, *322*, 376–391. [[CrossRef](#)]
35. Bird, D.K.; Brooks, K.C.; Gannicott, R.A.; Turner, P.A. A gold-bearing horizon in the Skaergaard intrusion, East Greenland. *Econ. Geol.* **1991**, *86*, 1083–1092. [[CrossRef](#)]
36. Garuti, G.; Fershtater, G.; Bea, F.; Montero, P.; Pushkarev, E.V.; Zaccarini, F. Platinum-group elements as petrological indicators in mafic-ultramafic complexes of the central and southern Urals: Preliminary results. *Tectonophysics* **1997**, *267*, 181–194. [[CrossRef](#)]
37. Ghose, N.C. Occurrence of native gold and gold-silver alloy in the olivine gabbro of layered cumulate sequence of Naga Hills ophiolite, India. *Curr. Sci.* **2014**, *106*, 1125–1130.
38. Kepezhinskas, P.; Kepezhinskas, N.; Berdnikov, N. Gold, palladium and platinum enrichments in arcs: Role of mantle wedge, arc crust and halogen-rich slab fluids. In Proceedings of the E3S Web Conference, Tomsk, Russia, 20–26 July 2019; Volume 98. [[CrossRef](#)]

39. Kepezhinskas, P.K.; Kepezhinskas, N.P.; Berdnikov, N.V.; Krutikova, V.O. Native metals and intermetallic compounds in subduction-related ultramafic rocks from the Stanovoy mobile belt (Russian Far East): Implications for redox heterogeneity in subduction zones. *Ore Geol. Rev.* **2020**, *127*, 3800. [[CrossRef](#)]
40. Brown, K.L. Gold deposition from geothermal discharges in New Zealand. *Econ. Geol.* **1986**, *81*, 979–983. [[CrossRef](#)]
41. Hedenquist, J.W.; Aoki, M.; Shinohara, H. Flux of volatiles and ore-forming metals from the magmatic-hydrothermal system of Satsuma Iwojima volcano. *Geology* **1994**, *22*, 585–588. [[CrossRef](#)]
42. Gammons, C.H.; Jones, W.A.E. Chemical mobility of gold in the porphyry-epithermal environment. *Econ. Geol.* **1997**, *92*, 45–59. [[CrossRef](#)]
43. Sillitoe, R.H.; Hedenquist, J.W. Linkages between volcanotectonic settings, pre-fluid compositions, and epithermal precious metal deposits. *Soc. Econ. Geol. Spec. Publ.* **2003**, *10*, 315–343.
44. Nadeau, O. Ore metals beneath volcanoes. *Nat. Geosci.* **2015**, *8*, 168–170. [[CrossRef](#)]
45. Zentilli, M.; Brooks, R.R.; Helgason, J.; Ryan, D.E.; Zhang, H. The distribution of gold in volcanic rocks of eastern Iceland. *Chem. Geol.* **1985**, *48*, 17–28. [[CrossRef](#)]
46. Togashi, S.; Terashima, S. The behavior of gold in unaltered island arc tholeiitic rocks from Izu-Oshima, Fuji, and Osoreyama volcanic areas, Japan. *Geochim. Cosmochim. Acta* **1997**, *61*, 543–554. [[CrossRef](#)]
47. Rosa, D.R.N. The incompatible behavior of gold in reduced magmas: A working hypothesis. *Comm. Geológicas* **2005**, *92*, 75–78.
48. Mustard, R.; Ulrich, T.; Kamenetsky, V.S.; Mernagh, T. Gold and metal enrichment in natural granitic melt during fractional crystallization. *Geology* **2006**, *34*, 85–88. [[CrossRef](#)]
49. Park, J.W.; Campbell, I.H.; Kim, J.; Moon, J.W. The role of late sulfide saturation in the formation of a Cu- and Au-rich magma: Insights from the platinum group element geochemistry of Niutahi-Motutahi lavas, Tonga Rear Arc. *J. Petrol.* **2015**, *56*, 59–81. [[CrossRef](#)]
50. Mungall, J.E.; Andrews, D.R.A.; Cabri, L.J.; Sylvester, P.J.; Tubrett, M. Partitioning of Cu, Ni, Au and platinum-group elements between monosulfide solid solution and sulfide melt under controlled oxygen and sulfur fugacities. *Geochim. Cosmochim. Acta* **2005**, *69*, 4349–4360. [[CrossRef](#)]
51. Botcharnikov, R.E.; Linnen, R.L.; Wilke, M.; Holtz, F.; Jugo, P.J.; Berndt, J. High gold concentrations in sulphide-bearing magma under oxidizing conditions. *Nat. Geosci.* **2011**, *4*, 112–115. [[CrossRef](#)]
52. Jégo, S.; Pichavant, M. Gold solubility in arc magmas: Experimental determination of the effect of sulfur at 1000 °C and 0.4 GPa. *Geochim. Cosmochim. Acta* **2012**, *84*, 560–592. [[CrossRef](#)]
53. Li, Y.; Feng, L.; Kiseeva, E.S.; Gao, Z.; Guo, H.; Du, Z.; Wang, F.; Shi, L. An essential role for sulfur in sulfide-silicate melt partitioning of gold and magmatic gold transport at subduction settings. *Earth Planet. Sci. Lett.* **2019**, *528*, 5850. [[CrossRef](#)]
54. Crocket, J.H.; Fleet, M.E.; Stone, W.E. Experimental partitioning of osmium, iridium and gold between basalt melt and sulphide liquid at 1300 °C. *Aust. J. Earth Sci.* **1992**, *39*, 427–432. [[CrossRef](#)]
55. Barnes, S.J. Partitioning of the platinum group elements and gold between silicate and sulphide magmas at Munni Munni Complex, Western Australia. *Geochim. Cosmochim. Acta* **1993**, *57*, 1277–1290. [[CrossRef](#)]
56. Simon, A.C.; Pettke, T.; Candela, P.A.; Piccoli, P.M.; Heinrich, C.A. The partitioning behavior of As and Au in S-free and S-bearing magmatic assemblage. *Geochim. Cosmochim. Acta* **2007**, *71*, 1764–1782. [[CrossRef](#)]
57. Zajacz, Z.; Candela, P.A.; Piccoli, P.M.; Walle, M.; Sanchez-Valle, C. Gold and copper in volatile saturated mafic and to intermediate magmas: Solubilities, partitioning, and implications for ore deposit formation. *Geochim. Cosmochim. Acta* **2012**, *91*, 140–159. [[CrossRef](#)]
58. Li, Y.; Audetat, A. Gold solubility and partitioning between sulfide liquid, monosulfide solid solution and hydrous mantle melts: Implications for the formation of Au-rich magmas and crust-mantle differentiation. *Geochim. Cosmochim. Acta* **2013**, *118*, 247–262. [[CrossRef](#)]
59. Nevstruev, V.G.; Berdnikov, N.V.; Didenko, A.N.; Saksin, B.G.; Lavrik, N.A. Fluidolites as a source of primary gold-platinum mineralization in the Poperechnoe Deposit (Malyi Khingan Range, Russia). *Dokl. Earth Sci.* **2018**, *482*, 1203–1206. [[CrossRef](#)]
60. Nevstruev, V.G.; Berdnikov, N.V.; Saksin, B.G. A new type of noble metal mineralization in fluidolites of the Poperechnoye Deposit, Lesser Khingan, Russia. *Russ. J. Pac. Geol.* **2019**, *13*, 51–60. [[CrossRef](#)]
61. Berdnikov, N.V.; Nevstruev, V.G.; Kepezhinskas, P.K.; Mochalov, A.G.; Yakubovich, O.V. PGE mineralization in andesite explosive breccias associated with the Poperechnoye iron-manganese deposit (Lesser Khingan, Far East Russia): Whole-rock geochemical, ¹⁹⁰Pt-⁴He isotopic, and mineralogical evidence. *Ore Geol. Rev.* **2020**, *118*, 3352. [[CrossRef](#)]
62. Egorov, E.V.; Timofeieva, M.W. Effusive iron-silica formations and iron-ore deposits of the Maly Khingan. In *Genesis of Iron and Manganese Deposits. Proceedings of Kiev Symposium*; UNESCO: Paris, France, 1973; pp. 181–185.
63. Berdnikov, N.V.; Nevstruev, V.G.; Saksin, B.G. Sources and formation conditions of ferromanganese mineralization of the Bureya and Khanka massifs, Russian Far East. *Russ. J. Pac. Geol.* **2016**, *10*, 263–273. [[CrossRef](#)]
64. Shatkov, G.A.; Volsky, A.S. *Tectonics, Deep Structure and Minerageny of the Amur Region and Adjacent Areas*; SPb VSEGEI Press: St. Petersburg, Russia, 2004; p. 190. (In Russian)
65. Wilde, S.A.; Wu, F.Y.; Zhao, G. The Khanka Block, NE China, and its significance for the evolution of the Central Asian Orogenic Belt and continental accretion. *Geol. Soc. Lond. Spec. Publ.* **2010**, *338*, 117–137. [[CrossRef](#)]

66. Luan, J.P.; Wang, F.; Xu, W.L.; Ge, W.C.; Sorokin, A.A.; Wang, Z.W.; Guo, P. Provenance, age, and tectonic implications of Neoproterozoic strata in the Jiamusi Massif: Evidence from U-Pb ages and Hf isotope compositions of detrital and magmatic zircons. *Precamb. Res.* **2017**, *297*, 19–32. [[CrossRef](#)]
67. Morrison, G.W. Characteristics and tectonic setting of the shoshonite rock association. *Lithos* **1980**, *13*, 97–108. [[CrossRef](#)]
68. Kepezhinskias, P. Diverse shoshonite magma series in the Kamchatka Arc: Relationships between intra-arc extension and composition of alkaline magmas. *Geol. Soc. Lond. Spec. Publ.* **1994**, *81*, 249–264. [[CrossRef](#)]
69. McDonough, W.F.; Sun, S.S. The composition of the Earth. *Chem. Geol.* **1995**, *120*, 223–253. [[CrossRef](#)]
70. Pearce, J.A. Trace element characteristics of lavas from destructive plate boundaries. *Andesites* **1982**, *8*, 525–548.
71. Pearce, J.A. Geochemical fingerprinting of oceanic basalts with applications to ophiolite classification and the search for Archean oceanic crust. *Lithos* **2008**, *100*, 14–48. [[CrossRef](#)]
72. Kepezhinskias, P.K.; Defant, M.J.; Drummond, M.S. Progressive enrichment of island arc mantle by melt-peridotite interaction inferred from Kamchatka xenoliths. *Geochim. Cosmochim. Acta* **1996**, *60*, 1217–1229. [[CrossRef](#)]
73. Wood, D.A. The application of a Th–Hf–Ta diagram to problems of tectonomagmatic classification and to establishing the nature of crustal contamination of basaltic lavas of the British Tertiary Volcanic Province. *Earth Planet. Sci. Lett.* **1980**, *50*, 11–30. [[CrossRef](#)]
74. Philpotts, A.R. Silicate liquid immiscibility in tholeiitic basalts. *J. Petrol.* **1979**, *20*, 99–118. [[CrossRef](#)]
75. Kjarsgaard, B.A.; Hamilton, D.L. Liquid immiscibility and the origin of alkali-poor carbonatites. *Mineral. Mag.* **1988**, *52*, 43–55. [[CrossRef](#)]
76. Honour, V.C.; Holness, M.B.; Partridge, J.L.; Charlier, B. Microstructural evolution of silicate immiscible liquids in ferrobasalts. *Contrib. Mineral. Petrol.* **2019**, *174*, 77. [[CrossRef](#)]
77. Wise, J. *Gold Recovery, Properties and Applications*; D. Van Nostrand Company: Taylorville, IL, USA, 1964; p. 167.
78. Greenwood, N.; Earnshaw, A. *Chemistry of the Elements*, 2nd ed.; Butterworth-Heinemann: Oxford, UK, 1997; p. 1359.
79. Perry, D.L. *Handbook of Inorganic Compounds*; CRC Press: Boca Raton, FL, USA, 1995; p. 354.
80. Yudovskaya, M.D.; Distler, V.V.; Chaplygin, I.V.; Mokhov, A.V.; Trubkin, N.V.; Gorbachev, S.A. Gaseous transport and deposition of gold in magmatic fluid: Evidence from the active Kudryavy volcano, Kurile Islands. *Mineral. Deposita* **2006**, *40*, 828–848. [[CrossRef](#)]
81. Chudnenko, K.V.; Pal'yanova, G.A. Thermodynamic properties of solid solutions in the Ag–Au–Cu system. *Russ. Geol. Geophys.* **2014**, *55*, 449–463. [[CrossRef](#)]
82. Knight, J.; Leitch, C.H.B. Phase relations in the system Au–Cu–Ag at low temperatures, based on natural assemblages. *Can. Mineral.* **2001**, *39*, 889–905. [[CrossRef](#)]
83. Neumann, J.P.; Zhong, T.; Chang, Y.A. The Cu–O (Copper–Oxygen) system. *Bull. Alloy Phase Diagr.* **1984**, *5*, 136–140. [[CrossRef](#)]
84. Reid, S.J.B. *Electron Microprobe Analysis and Scanning Electron Microscopy in Geology*; Cambridge University Press: Cambridge, UK, 2005; p. 212.
85. Berdnikov, N.V.; Konovalova, N.S.; Zazulina, V.Y. Investigation of precious metal inclusions in highly carbonaceous rocks by the SEM and X-ray spectrum analysis methods. *Russ. J. Pac. Geol.* **2010**, *4*, 164–170. [[CrossRef](#)]
86. Goldstein, J.I.; Newbury, D.E.; Michael, J.R.; Ritchie, N.W.M.; Scott, J.H.J.; Joy, D.C. *Scanning Electron Microscopy and X-ray Microanalysis*; Springer: New York, NY, USA, 2017; p. 550.
87. Fredriksson, H.; Akerling, U. *Solidification and Crystallization Processing in Metals and Alloys*; John Wiley & Sons Ltd.: London, UK, 2012; p. 826.
88. Gavrilin, I.V. *Melting and Crystallization of Metals and Alloys*; Vladimir State University: Vladimir, Russia, 2000; p. 260. (In Russian)
89. Munitz, A.; Venkert, A.; Landau, P.; Kaufman, M.J.; Abbaschian, R. Microstructure and phase selection in supercooled copper alloys exhibiting metastable liquid miscibility gaps. *J. Mater. Sci.* **2012**, *47*, 7955–7970. [[CrossRef](#)]
90. Lidin, R.R.; Andreeva, L.L.; Molotchko, V.A. *Handbook of Constants for Inorganic Compounds*; Drofa Publishers: Moscow, Russia, 2006; p. 685. (In Russian)
91. Lamiri, I.; Abdelbaky, M.S.M.; Hamana, D.; Granda, G.S. Metastable phase in binary and ternary 12-carat gold alloys at low temperature. *Mater. Res. Express* **2018**, *5*, 6506. [[CrossRef](#)]
92. Zhang, J.; Li, Y. Effects of different rotation speeds on microstructure, hardness and corrosion resistance of the Au–Cu alloy. *Gold Bull.* **2017**, *50*, 137–145. [[CrossRef](#)]
93. Pezzato, L.; Magnabosco, G.; Brunelli, K. Microstructure and mechanical properties of a 18 Kt 5N gold alloy after different heat treatments. *Metallogr. Microstruct. Anal.* **2016**, *5*, 116–123. [[CrossRef](#)]
94. Pakhomova, V.A.; Zalischak, B.L.; Korzhinskaya, V.S.; Afanasieva, T.B.; Lapina, M.I. Genetic peculiarities of the formation of helzircon–baddeleyite ores based on thermobarogeochemical data (a case study of the Algama deposit, Khabarovsk region). In *Ore Deposits at Continental Margins*; Dalnauka: Vladivostok, Russia, 2000; pp. 248–262. (In Russian)
95. Korzhinskaya, V.S.; Nekrasov, I.Y. Stability of the association ZrSiO₄–SiO₂–ZrO₂ in alkaline solutions at temperature of 500 °C and pressure of 1 kbar. *Dokl. Earth Sci.* **1998**, *359*, 205–207.
96. Ozolins, V.; Wolverson, C.; Zunger, A. Cu–Au, Ag–Au, Cu–Ag and Ni–Au intermetallics: First-principles study of phase diagrams and structures. *Phys. Rev. B. Cond. Matter* **1998**, *57*, 6427–6443. [[CrossRef](#)]
97. Andrieux, J.; Dezellus, O.; Bosselet, F.; Peronnet, S.M.; Sigala, C.; Chirioc, R.; Viala, J.C. Details on the formation of Ti₂Cu₃ in the Ag–Cu–Ti system in the temperature range 790–860 °C. *J. Phase Equil. Diffus.* **2008**, *29*, 156–162. [[CrossRef](#)]

98. Murray, J.L. *Phase Diagrams of Binary Titanium Alloys*; ASM International: Geauga, OH, USA, 1987; p. 345.
99. Pal'yanova, G.A.; Kokh, K.A.; Seryotkin, Y.V. Formation of gold-silver sulfides and native gold in Fe-Ag-Au-S system. *Russ. Geol. Geophys.* **2012**, *53*, 347–355. [[CrossRef](#)]
100. Cook, N.J.; Chryssoulis, S.L. Concentrations of “invisible gold” in the common sulfides. *Can. Mineral.* **1990**, *28*, 1–16.
101. Barnes, S.J.; Cox, R.J.; Zientek, M.L. Platinum-group element, gold, silver and base metal distribution in compositionally zoned sulfide droplets from the Medvezky Creek Mine, Noril'sk, Russia. *Contrib. Mineral. Petrol.* **2006**, *152*, 187–200. [[CrossRef](#)]
102. Zelenski, M.; Kamenetsky, V.S.; Mavrogenes, J.A.; Danyushevsky, L.V.; Matveev, D.; Gurenko, A.A. Platinum-group elements and gold in sulfide melts from modern arc basalt (Tolbachik volcano, Kamchatka). *Lithos* **2017**, *290–291*, 172–188. [[CrossRef](#)]
103. Trubac, J.; Ackerman, L.; Gauert, C.; Durisova, J.; Hrstka, T. Platinum-group elements and gold in base metal sulfides, platinum-group minerals, and Re-Os isotope compositions of the Uitkomst Complex, South Africa. *Econ. Geol.* **2018**, *113*, 439–461. [[CrossRef](#)]
104. Frank, M.R.; Candela, P.A.; Piccoli, P.M.; Glascock, M.D. Gold solubility, speciation, and partitioning as a function of HCl in the brine-silicate melt-metallic gold system at 800 °C and 100 MPa. *Geochim. Cosmochim. Acta* **2002**, *66*, 3719–3732. [[CrossRef](#)]
105. Sullivan, N.A.; Zajacz, Z.; Brenan, J.M. The solubility of Pd and Au in hydrous intermediate silicate melts: The effect of oxygen fugacity and the addition of Cl and S. *Geochim. Cosmochim. Acta* **2018**, *231*, 15–29. [[CrossRef](#)]
106. Jégo, S.; Nakamura, M.; Kimura, J.I.; Iizuka, Y.; Chang, Q.; Zellmer, G.F. Is gold solubility subject to pressure variations in ascending arc magmas? *Geochim. Cosmochim. Acta* **2016**, *188*, 224–243. [[CrossRef](#)]
107. Wernette, B.; Li, P.; Boudreau, A. Sulfides, native metals, and associated trace minerals of the Skaergaard intrusion, Greenland: Evidence for late hydrothermal fluids. *Mineral. Deposita* **2020**, *55*, 1197–1214. [[CrossRef](#)]
108. Cameron, E.M.; Hattori, K. Archean gold mineralization and oxidized hydrothermal fluids. *Econ. Geol.* **1987**, *82*, 1177–1191. [[CrossRef](#)]
109. Heald, P.; Foley, N.K.; Hayba, D.O. Comparative anatomy of volcanic-hosted epithermal deposits: Acid sulfate and adularia-sericite types. *Econ. Geol.* **1987**, *82*, 1–26. [[CrossRef](#)]
110. Simmons, S.F.; Browne, P.R.L. Mineralogic, alteration and fluid-inclusion studies of epithermal gold-bearing veins at the Mt. Muro Prospect, Central Kalimantan (Borneo), Indonesia. *J. Geochem. Explor.* **1990**, *35*, 63–103. [[CrossRef](#)]
111. Rye, R.O. The evolution of magmatic fluids in the epithermal environment: The stable isotope perspective. *Econ. Geol.* **1993**, *88*, 733–752. [[CrossRef](#)]
112. Pal'yanova, G.A.; Kolonin, G.R. Geochemical mobility of Au and Ag during hydrothermal transfer and precipitation: Thermodynamic simulation. *Geochem. Int.* **2007**, *45*, 744–757. [[CrossRef](#)]
113. Yesares, L.; Aiglsperger, T.; Sáez, R.; Almodóvar, G.R.; Nieto, J.M.; Proenza, J.A.; Gómez, C.; Escobar, J.M. Gold behavior in supergene profiles under changing redox conditions: The example of the Las Cruces deposit, Iberian Pyrite Belt. *Econ. Geol.* **2015**, *110*, 1–18. [[CrossRef](#)]
114. Ballhaus, C.; Sylvester, P. Noble metal enrichment processes in the Merensky Reef, Bushveld Complex. *J. Petrol.* **2000**, *41*, 545–561. [[CrossRef](#)]
115. Anenburg, M.; Mavrogenes, J.A. Noble metal nanonugget insolubility in geological sulfide liquids. *Geology* **2020**, *48*, 939–943. [[CrossRef](#)]
116. Nielsen, T.F.D.; Andersen, J.C.Ø.; Holness, M.B.; Keiding, J.K.; Rudashevsky, N.S.; Rudashevsky, V.N.; Salmonsén, L.P.; Tegner, C.; Veksler, I.V. The Skaergaard PGE and gold deposit: The result of *in situ* fractionation, sulphide saturation, and magma chamber-scale precious metal redistribution. *J. Petrol.* **2015**, *56*, 1643–1676. [[CrossRef](#)]
117. Borisov, A.A.; Palme, H. Solubilities of noble metals in Fe-containing silicate melts as derived from experiments in Fe-free systems. *Amer. Mineral.* **2000**, *85*, 1665–1673. [[CrossRef](#)]
118. Widom, E.; Kepezhinskis, P.; Defant, M.J. The nature of metasomatism in the sub-arc mantle wedge: Evidence from Re-Os isotopes in Kamchatka peridotite xenoliths. *Chem. Geol.* **2003**, *196*, 283–306. [[CrossRef](#)]
119. Kiseeva, E.S.; Fonseca, R.O.C.; Smythe, D.J. Chalcophile elements and sulfides in the upper mantle. *Elements* **2017**, *13*, 111–116. [[CrossRef](#)]
120. Lugué, A.; Pearson, G. Dating mantle peridotites using Re-Os isotopes: The complex message from whole rocks, base metal sulfides, and platinum group minerals. *Am. Mineral.* **2019**, *104*, 165–189. [[CrossRef](#)]
121. Hattori, K. High-sulfur magma, a product of fluid discharge from underlying mafic magma: Evidence from Mount Pinatubo, Philippines. *Geology* **1993**, *21*, 1083–1086. [[CrossRef](#)]
122. Larocque, A.C.L.; Stimac, J.A.; Keith, J.D.; Huminicki, M.A.E. Evidence for open-system behavior in immiscible Fe-S-O liquids in silicate magmas: Implications for contributions of metals and sulfur to ore-forming fluids. *Can. Mineral.* **2000**, *38*, 1233–1249. [[CrossRef](#)]
123. Georgatou, A.A.; Chiaradia, M. Magmatic sulfides in high-potassium calc-alkaline to shoshonitic and alkaline rocks. *Solid Earth* **2020**, *11*, 1–21. [[CrossRef](#)]
124. Métrich, N.; Mandeville, C.W. Sulfur in magmas. *Elements* **2010**, *6*, 81–86. [[CrossRef](#)]
125. Lawley, C.J.M.; Petts, D.C.; Jackson, S.E.; Zagorevski, A.; Pearson, D.G.; Kjarsgaard, B.A.; Savard, D.; Tschirhart, V. Precious metal mobility during serpentinization and breakdown of base metal sulphide. *Lithos* **2020**, *354–355*, 105278. [[CrossRef](#)]
126. Buisson, G.; Leblanc, M. Gold in mantle peridotites from Upper Proterozoic ophiolites in Arabia, Mali, and Morocco. *Econ. Geol.* **1987**, *82*, 2091–2097. [[CrossRef](#)]

127. Lorand, J.P.; Alard, O.; Luguët, A. Platinum-group element micronuggets and refertilization process in Lherz orogenic peridotite (northeastern Pyrenees, France). *Earth Planet. Sci. Lett.* **2010**, *289*, 298–310. [[CrossRef](#)]
128. Krieger, P.; Hagner, A.F. Gold-nickel mineralization at Alistos, Sinaloa, Mexico. *Am. Mineral.* **1943**, *28*, 257–271.
129. Sluzhenikin, S.F.; Mokhov, A.V. Gold and silver in PGE-Cu-Ni and PGE ores of the Noril'sk deposits, Russia. *Mineral. Depos.* **2015**, *50*, 465–497. [[CrossRef](#)]
130. Helmy, H.M.; Ballhaus, C.; Fonseca, R.O.C.; Wirth, R.; Nagel, T.J.; Tredoux, M. Noble metal nanoclusters and nanoparticles precede mineral formation in magmatic sulfide melts. *Nat. Commun.* **2013**, *4*, 2405. [[CrossRef](#)] [[PubMed](#)]
131. Peregoedova, A.; Barnes, S.J.; Baker, D.R. The formation of Pt-Ir alloys and Cu-Pd-rich sulfide melts by partial desulfurization of Fe-Ni-Cu sulfides: Results of experiments and implications for natural systems. *Chem. Geol.* **2004**, *208*, 247–264. [[CrossRef](#)]
132. Williams, P.J.; Barton, M.D.; Johnson, D.A.; Fontbote, L.; de Haller, A.; Mark, G.; Oliver, N.H.S.; Marschik, R. Iron oxide copper-gold deposits: Geology, space-time distribution and possible modes of origin. *Econ. Geol.* **2005**, *100*, 371–405.
133. Naslund, R.H.; Henriquez, F.; Nyström, J.O.; Vivallo, W.; Dobbs, F.M. Magmatic iron ores and associated mineralization: Examples from the Chilean High Andes and Coastal Cordillera. In *Hydrothermal Iron Oxide-Copper-Gold & Related Deposits: A Global Perspective*; Porter, T.M., Ed.; PGC Publishing: Adelaide, Australia, 2002; Volume 2, pp. 207–226.
134. Sillitoe, R.H. Iron oxide-copper-gold deposits: An Andean view. *Mineral. Depos.* **2003**, *38*, 787–812. [[CrossRef](#)]
135. Ootes, L.; Snyder, D.; Davis, W.J.; Gongora, A.P.; Corriveau, L.; Mumin, A.; Gleeson, S.A.; Samson, I.M.; Montreuil, J.F.; Potter, E.; et al. A Paleoproterozoic Andean-type iron-oxide copper-gold enrichment, the Great Bear magmatic zone, Northwest Canada. *Ore Geol. Rev.* **2017**, *81*, 123–139. [[CrossRef](#)]
136. Barra, F.; Reich, M.; Rojas, P.; Selby, D.; Simon, A.C.; Salazar, E.; Palma, G. Unraveling the origin of the Andean IOCG Clan: A Re-Os isotope approach. *Ore Geol. Rev.* **2017**, *81*, 62–78. [[CrossRef](#)]
137. Zhu, Z. Gold in iron oxide copper-gold deposits. *Ore Geol. Rev.* **2016**, *72*, 37–42. [[CrossRef](#)]
138. Childress, T.M.; Simon, A.C.; Reich, M.; Barra, F.; Arce, M.; Lundstrom, C.C.; Bindeman, I.N. Formation of the Mantoverde iron oxide-copper-gold (IOCG) deposit, Chile: Insights from Fe and O stable isotopes and comparisons with iron oxide-apatite (IOA) deposits. *Mineral. Depos.* **2020**, *55*, 1489–1504. [[CrossRef](#)]
139. Barton, M.D.; Johnson, D.A. Evaporitic-source model for igneous-related Fe oxide-(REE-Cu-Au-U) mineralization. *Geology* **1996**, *26*, 259–262. [[CrossRef](#)]
140. Benavides, J.; Kyser, T.K.; Clark, A.H.; Oates, C.J.; Zamora, R.; Tarnovschi, R.; Castillo, B. The Mantoverde iron oxide-copper-gold district, III Región, Chile: The role of regionally derived, non-magmatic fluids in chalcopyrite mineralization. *Econ. Geol.* **2007**, *102*, 415–440. [[CrossRef](#)]
141. Barton, M.D. Iron oxide (-Cu-Au-REE-P-Ag-U-Co) systems. In *Geochemistry of Mineral Deposits*, 2nd ed.; Scott, S.D., Ed.; Treatise on Geochemistry; Elsevier: Amsterdam, The Netherlands, 2013; Volume 13, pp. 515–541.
142. Pollard, P.J. An intrusion-related origin for Cu-Au mineralization in iron oxide-copper-gold (IOCG) provinces. *Mineral. Depos.* **2006**, *41*, 179–187. [[CrossRef](#)]
143. Tornos, F.; Velasco, F.; Barra, F.; Morata, D. The Tropezón Cu-Mo-(Au) deposit, Northern Chile: The missing link between IOCG and porphyry copper systems? *Mineral. Depos.* **2010**, *45*, 313–321. [[CrossRef](#)]
144. Richards, J.P.; Mumin, A.H. Magmatic-hydrothermal processes within an evolving Earth: Iron oxide-copper-gold and porphyry Cu ± Mo ± Au deposits. *Geology* **2013**, *41*, 767–770. [[CrossRef](#)]
145. Groves, D.I.; Bierlein, F.P.; Meinert, L.D.; Hitzman, M.W. Iron oxide-copper-gold (IOCG) deposits through Earth history: Implications for origin, lithospheric setting, and distinction from other epigenetic iron oxide deposits. *Econ. Geol.* **2010**, *105*, 641–654. [[CrossRef](#)]
146. Chiaradia, M.; Banks, D.; Clift, R.; Marschik, R.; de Haller, A. Origin of fluids in iron oxide-copper-gold deposits: Constraints from $\delta^{37}\text{Cl}$, $^{87}\text{Sr}/^{86}\text{Sr}_i$, and Cl/Br. *Mineral. Depos.* **2006**, *41*, 565–573. [[CrossRef](#)]
147. Sillitoe, R.H. Porphyry copper systems. *Econ. Geol.* **2010**, *105*, 3–41. [[CrossRef](#)]
148. Kouzmanov, K.; Pokrovsky, G.S. Hydrothermal controls on metal distribution in porphyry Cu(-Mo-Au) systems. *Soc. Econ. Geol. Spec. Publ.* **2012**, *16*, 573–618.
149. Wilkinson, J.J. Triggers for the formation of porphyry ore deposits in magmatic arcs. *Nat. Geosci.* **2013**, *6*, 917–925. [[CrossRef](#)]
150. Heinrich, C.A.; Driesner, T.; Stefansson, A.; Seward, T.M. Magmatic vapor contraction and the transport of gold from the porphyry environment to epithermal ore deposits. *Geology* **2004**, *32*, 761–764. [[CrossRef](#)]
151. Kesler, S.E.; Chryssoulis, S.L.; Simon, G. Gold in porphyry copper deposits: Its abundance and fate. *Ore Geol. Rev.* **2002**, *21*, 103–124. [[CrossRef](#)]